Computational Fluid Dynamics Based Mixing Prediction for Tilt Pad Journal Bearing TEHD Modeling—Part I: TEHD-CFD Model Validation and Improvements

Jongin Yang
Mem. ASME
Department of Mechanical Engineering,
Texas A&M University,
College Station, TX 77840
e-mail: jiyang@tamu.edu

Alan Palazzolo
Department of Mechanical Engineering,
Texas A&M University,
College Station, TX 77840
e-mail: a-palazzolo@tamu.edu

The core contributions of Part I (1) present a computational fluid dynamics (CFD)-based approach for tilting pad journal bearing (TPJB) modeling including thermo-elasto hydrodynamic (TEHD) effects with multi-mode pad flexibility, (2) validate the model by comparison with experimental work, and (3) investigate the limitations of the conventional approach by contrasting it with the new approach. The modeling technique is advanced from the author's previous work by including pad flexibility. The results demonstrate that the conventional approach of disregarding the three-dimensional flow physics between pads (BP) can generate significantly different pressure, temperature, heat flux, dynamic viscosity, and film thickness distributions, relative to the high-fidelity CFD model. The uncertainty of the assumed mixing coefficient (MC) may be a serious weakness when using a conventional, TPJB Reynolds model, leading to prediction errors in static and dynamic performance. The advanced mixing prediction method for "BP" thermal flow developed in Part I will be implemented with machine learning techniques in Part II to provide a means to enhance the accuracy of conventional Reynolds based TPJB models.
[DOI: 10.1115/1.4047750]

Keywords: fluid film lubrication, hydrodynamic lubrication, journal bearings, thermoelastohydrodynamic lubrication

1 Introduction

The tilting pad journal bearing (TPJB) is the most widely utilized bearing in industry due to its superior dynamic stability. Accurate performance prediction of the TPJB is imperative for ensuring satisfactory machine reliability. Improved prediction accuracy is increasingly relying on greater sophistication of modeling algorithms and computational methods and hardware. The thin-film Reynolds model for solving approximate continuity and momentum equations has been the basis for the conventional TPJB modeling method [1–34]. More recently, the computational fluid dynamics (CFD) method has been applied to TPJB modeling [42–52].

Conventional (Reynolds equation) TPJB modeling has evolved using increasingly sophisticated and comprehensive features since the 1964 paper on the TPJB dynamic coefficient evaluation by Lund [1], as summarized in Table 1. These features include use of a generalized (variable viscosity) Reynolds equation, and a three-dimensional (3D) energy equation (film, shaft, and pad), inclusion of 3D structural features (shaft, pad), pivot flexibility, mixing theory, frequency reduced dynamic coefficients, and multiple-mode pad flexibility effects. The works of numerous researchers have revealed that the static and dynamic properties of TPJB are strongly influenced by the above features and combinations of them. The multiphysics nature and increasingly complex geometries of the evolved TPJB models required advancements in computational hardware and algorithms. Tremendous strides in improving TPJB modeling accuracy and efficiency have been accomplished in the past 50 years. This is highlighted in Refs. [1–34], which may inadvertently exclude some excellent papers for the sake of brevity.

The following is a brief discussion of the papers listed in Table 1. Lund [1] introduced the concept of synchronously (or frequency) reduced dynamic coefficients, which subsequently has been utilized as "standard practice." Some machinery acceptance standards, such as American Petroleum Institute (API) 617 for process compressors, require that simulations for resonance, stability, etc., utilize frequency (synchronously) reduced dynamic coefficients for bearing stiffness and damping. Tieu [2] established the importance of thermal effects using finite element-based solutions of the energy equation for lubricant temperature and the variable viscosity Reynolds equation.

The importance of including pivot deflection for improving dynamic coefficient accuracy has been identified by Kirk and Reedy [4], Brugier and Pascal [6], Medhi et al. [19], and San Andres and Tao [21]. Ettles [3], Brugier and Pascal [6], Kim et al. [10,11], San Andres and Li [23], Suh and Palazzolo [30], and Gaines and Childs [34] improved TPJB modeling by considering thermal, pressure, and centrifugal load deformation of the TPJB, including shaft and pad temperature prediction. Fillon et al. [9] showed that the deformation of all bearing elements (shaft, pads, and housing) should be taken into account based on the experimental data under various operating conditions. Earles et al. [7], Kim et al. [11], and Suh and Palazzolo [30] advanced TPJB dynamic coefficient modeling by including two-dimensional (2D) and three-dimensional (3D) modal coordinate for dynamic deformations. Approximate turbulence corrections to the laminar Reynolds thin-film model were introduced by Taniguchi et al. [8] and Arihara et al. [20]. Transient TPJB load modeling, e.g., due to blade loss, was the focus of Gadangi and Palazzolo [12], Desbordes et al. [13], and Haugaard and Santos [15].

Contributed by the Tribology Division of ASME for publication in the JOURNAL OF TRIBOLOGY. Manuscript received August 9, 2019; final manuscript received June 22, 2020; published online August 3, 2020. Assoc. Editor: Daejong Kim.

Table 1 Development history of TPJB performance prediction

Researchers\Newest Techniques	Generalized Reynolds	3D Film Energy	3D Shaft Energy	3D Pad Energy	Shaft Thermal 3D Deflection	Pad Thermal 3D Deflection	3D Pad Flexibility	Pivot Flexibility	Mixing Theory	Multiple-mode pad flexibility
Lund (1964) [1]	Δ	X	X	X	X	X	X	X	X	Δ
Tieu (1973) [2]	Δ	Δ	X	X	X	X	X	X	X	X
Ettles (1980) [3]	Δ	Δ	Δ	Δ	X	Δ	Δ	X	O	Δ
Knight and Barrett (1987) [5]	Δ	Δ	X	Δ	X	X	X	X	O	Δ
Brugier and Pascal (1989) [6]	O	O	X	Δ	O	O	O	O	O	Δ
Earles et al. (1990) [7]	Δ	X	X	X	X	X	O	O	O	Δ
Taniguchi et al. (1990) [8]	Δ	O	X	O	X	X	X	X	O	X
Kim et al. (1994–1995) [10,11]	O	Δ	X	Δ	X	Δ	Δ	O	O	O
Gadangi and Palazzolo (1995) [12]	O	Δ	X	X	X	X	Δ	X	X	X
Desbordes et al. (1995) [13]	Δ	X	X	X	X	X	O	X	X	X
Haugaard and Santos (2010) [15]	Δ	X	X	X	X	X	O	X	X	X
Rindi et al. (2015) [16]	Δ	X	X	X	X	X	X	O	X	X
Dang et al. (2017) [17]	Δ	Δ	O	O	X	O	O	O	X	Δ
Lee et al. (2018) [18]	O	O	X	O	X	X	X	X	O	X
Mehdi et al. (2018) [19]	Δ	Δ	X	X	X	X	X	O	O	X
Arihara et al. (2019) [20]	O	O	Δ	O	Δ	O	O	X	O	X
Andres et al. (2013–2019) [21–25]	Δ	Δ	X	X	Δ	Δ	Δ	O	O	X
Hagemann et al. (2017–2019) [26–29]	O	O	Δ	O	O	O	O	O	O	Δ
Palazzolo et al. (2014–2017) [30–33]	O	O	O	O	O	O	O	O	O	O

Note: *O: considered; Δ: simplified; and X: not considered.

In the case of the spherical-type pivot, the pivot friction effect may be significant for the static and dynamic performance prediction of a TPJB. Several studies [35–40] have been conducted theoretically and experimentally for investigating the pivot friction effect. In a recent study, Kim and Palazzolo [40] examined the nonlinear dynamic characteristics of a rotor-bearing system with the pivot friction effect, employing the Stribeck curve model [41] for accurate dynamic force and moment predictions on the pad.

Additional improvements to TPJB modeling were made in the areas of controllable oil injection [15], manufacturing uncertainty [17], wear on the bearing surface [18], starvation flow [24], etc. Fillon and Khonsari [14] provided thermo-hydro-dynamic (THD) design charts for the TPJB based on theoretical modeling. Advanced TPJB models in the recent literature [26–33] combine the above features with 3D numerical analysis.

There is, however, a general acknowledgment of weakness in prescribing accurate temperature boundary conditions at pad inlets [26,29,46,51,52] and modeling the cavitational flow and fluid inertia-dominant flow. Cavitation frequently occurs in diverging film or textured surfaces, and the phase change rates by evaporation and condensation are ignored in the conventional cavitation model (Reynolds equation). In particular, the conventional approach obtains a bulk flow approximation of a uniform temperature over the entire pad inlet due to the mixing of hot oil carryover from the preceding pad and fresh supply oil routed to the bearing. This approach is characterized by a MC which can only be empirically derived from experiment or by using a 3D Navier–Stokes—Thermal model solved with CFD techniques. As in Eq. (1), the MC mathematically is defined by the pad inlet (BP outlet) temperature, the supply oil temperature, and the outlet (BP inlet) temperature of the previous pad.

$$MC \equiv \frac{T_{out} - T_{\sup}}{T_{in} - T_{\sup}} = f(MC_k, Q_{in}, Q_{out}, \dots) \tag{1}$$

The MC can be expressed as a function of the assumed MC value (MC_k), BP inlet flowrate (Q_{in}), and BP outlet flowrate (Q_{out}).

The CFD approach reveals that the assumption of a uniform film temperature at the pad inlet is poor, especially in forced lubrication systems that employ nozzles and jets. However, this convention is utilized in most of the literature cited in Table 1. As a consequence, CFD has been adapted in recent publications [42–45]. Plain journal bearing models with full Navier–Stokes equation solutions, including thermal effects, and thermo-elastic deformation (fluid-structure interaction (FSI)) have been developed. Table 2 provides a summary of TPJB-related publications employing CFD, illustrating the contribution of the present work.

Most of these papers treat the TPJB with the assumption of isolated pads, neglect mesh deformation when considering pad and shaft motions, and neglect thermo-elastic deformation resulting from the solution of the three-dimensional energy equation. Armentrout et al. [47] proposed a hybrid CFD-Reynolds model, utilizing a Reynolds model for the shaft and pad equilibrium, but neglected thermal effects. Hagemann et al. [50] also utilized the initial film thickness from the solution of the thermo-elasto-hydrodynamic (TEHD) Reynolds model. However, both models were not fully coupled, resulting in a possible discontinuity in pressure, temperature, film thickness, etc., as discussed in Ref. [51]. Yang and Palazzolo [51] presented a significant improvement in the CFD modeling approach incorporating many modeling features of advanced Reynolds models, plus replacing the simple MC theory with full 3D, CFD-thermal modeling between pads (BP). Pad flexibility is known to reduce TPJB damping significantly [6,11,31,23,34] but was ignored in Ref. [51].

The objectives of Part I are to (1) improve the TEHD CFD model by including pad flexibility and investigate its effect on the static and dynamic prediction accuracy, (2) present the detailed methodology for the TEHD-CFD model with pad flexibility, (3) validate the approach by comparison with experimental results [53,54], and (4) investigate the limitations of the conventional (Reynolds) approach's by comparing the temperature, pressure, heat flux, and film thickness fields with the CFD results. Part II demonstrates how the conventional approach may be improved by using artificial neural networks in machine learning to utilize CFD flow model results to represent pad inlet temperature distributions more accurately.

Table 2 Recent CFD researches and modeling technique for TPJB

Researchers\Newest Techniques	Full-Bearing (1)	Mesh Deformation (2)	Shaft & Pads Equilibrium (3)	Film Energy (4)	Shaft Energy (5)	Pad Energy (6)	Shaft Thermal Deflection (7)	Pad Thermal Deflection (8)	Pad Flexibility (9)	Pivot Flexibility (10)	Transitional Turbulence (11)	Multiphase w/ Cavitation (12)	Multiple-mode Pad Flexibility (13)
Li et al. (2016) [46]	O	O	O	X	X	X	X	X	X	X	X	X	Δ
Armentrout et al. (2017) [47]	X	X	Δ	X	X	X	X	X	X	X	Δ	X	X
Crone et al. (2018) [48]	X	O	Δ	O	X	O	X	X	X	X	Δ	X	X
Ding et al. (2018) [49]	O	X	X	O	X	X	X	X	X	X	Δ	O	X
Hagemann et al. (2018–2019) [29,50]	X	X	O	O	X	O	X	O	X	X	X	X	X
Yang and Palazzolo (2019) [51,52]	O	O	O	O	O	O	O	O	X	O	O	O	Δ
Yang and Palazzolo (present study)	O	O	O	O	O	O	O	O	O	O	O	O	O

Note: O: considered; Δ: simplified; and X: not considered.

Fig. 1 TPJB configuration for the CFD model

2 TEHD–CFD Modeling Methodology Including Pad Flexibility

2.1 Pad Flexibility Consideration. The author's prior work [51,52] presents a CFD modeling methodology for TPJB static and dynamic performance prediction, including 3D multiphase flow, thermal-fluid, transitional turbulence, thermal-rotational shaft, and thermal deformation of the shaft and pads using FSI techniques. The k–ω-based shear stress transport (SST) model with an additional two equations is applied to solve the Reynolds-averaged Navier–Stokes (RANS) equations with the Reynolds stress terms. The gamma transitional turbulence model was also included for the laminar and turbulence transition between pads.

The model considers shaft translational motion, pad tilting motion, and pivot flexibility. Pad flexibility was neglected in Refs. [51,52], but it is included in the present study.

The TPJB system has five pads with the load between pads (LBP), as shown in Fig. 1. The BP region is groove region between pads and its detailed model is a distinguishable feature of the present CFD model. The fluid-film domain (blue) is divided into the five sub-domains on each pad. Determination of bearing damping requires specification of equivalent mass, momentum, and energy source terms corresponding to velocity perturbations of the rotor-bearing coordinates. The source terms are local to five sub-domains that are defined in the CFX model. Velocity perturbations of selected mode shapes are performed to obtain damping coefficients and are prescribed as source terms in the conservation equations for the fluid film sub-domains (blue). The pad

Fig. 2 Multiphysics static calculation for the flexible pad case

Fig. 3 Multiphysics dynamics calculation for the flexible pad case

mesh is displaced by perturbing the modal coordinates of selected eigenvectors of the flexible pad. These pad displacement perturbations of the pad surfaces (red) are imposed as boundary conditions on the fluid film. Figures 2 and 3 illustrate the codes employed in the multiphysics solution process for both the static and dynamics cases, respectively. Figure 2 shows that the pressure distribution at the pad surface, from the CFD solver, is transferred to the finite element analysis (FEA) solver to determine deflections during the iterative calculation for the static solution.

Figure 3 shows the computational procedure for calculating dynamic coefficients, including CFD thermal and flow modeling and pad flexibility effects. First, the selected modes, pad geometry, and properties are input in the 3D structure model. Then, the stiffness and mass matrix is assembled based on the finite element method (FEM) [55], and the eigenvectors (mode shapes) of the pads are calculated. The selected mode shapes are utilized to perturb the pad surface displacements in the CFD solver to obtain the resulting perturbed forces, which are formed as resultants of pressures and shear stresses acting on the pads surfaces. The perturbed forces are transferred from the CFD solver to the 3D structure (FEM) code, where they are interpolated on the pad surface nodes. The perturbed forces are utilized to calculate the full set of un-reduced dynamic coefficients, after transforming coordinates from physical to modal. Ultimately, the frequency reduced dynamic coefficients are determined, and subsequently, log decrements and other system dynamic response types are obtained.

2.2 Stiffness and Damping Matrices, and Log Decrement (Finite Element Analysis Solver). The perturbation method for CFD evaluation of dynamic coefficients was presented in Ref. [52] for the rigid pad case. The 12 degrees-of-freedom associated with a single, rigid pad TPJB include x and y translational journal motions, five pad pivot motions, and five tilting motions. Thus, 24 position perturbations, including both positive and negative ones, are needed for evaluating the bearing stiffness matrix, and 24 velocity perturbations are needed for evaluating the bearing damping matrix. Including pad flexibility requires modal coordinates for the pad deformation motion, which increases the total number of degrees-of-freedom. The number of pad modes included in the model is selected by balancing computational efficiency and accuracy, as described in Sec. 2.5. The mechanical APDL solver is used for static analysis, but an in-house 3D structure model is utilized for the dynamic coefficient calculation to achieve better compatibility among the solvers. The equation of motion for the undamped 3D pad structural model is

$$\underset{(n\times n)}{[m_p]}\,\underset{(n\times 1)}{\{\ddot{x}_p\}}+\underset{(n\times n)}{[k_p]}\,\underset{(n\times 1)}{\{x_p\}}=\underset{(n\times 1)}{\{f_p\}} \tag{2}$$

The mass $[m_p]$ and stiffness $[k_p]$ matrices are obtained using the FEM [55], and n indicates the number of degrees-of-freedom in the pad FEM mesh. The targeted bearing in this study has a cylindrical pivot. Thus, fixed displacements are imposed at axial line-nodes at the pivot location. Axial line nodes at the middle of pad surfaces are prescribed with a free boundary condition in the y'-direction (local coordinate, Fig. 4(*b*)), and fixed for other directions to prevent matrix singularity problems. The equations of motion become uncoupled when transformed into modal coordinates. Perturbation of the modal coordinates results in perturbations of the physical coordinates on the pad's film surface, via transformation from modal to physical coordinates. The mode shape vectors are derived in the usual manner from the free vibration form of Eq. (2)

$$\left(\underset{(n\times n)}{[k_p]}-\underset{(n\times n)}{[\lambda_p]}\,\underset{(n\times n)}{[m_p]}\right)\underset{(n\times n)}{[\phi_p]}=\left([k_p]-\begin{bmatrix}\lambda_{p1} & & 0\\ & \ddots & \\ 0 & & \lambda_{pn}\end{bmatrix}\right)[m_p]\Big)\Big[\underset{(n\times 1)}{\phi_{p1}}\,|\cdots|\,\underset{(n\times 1)}{\phi_{pn}}\Big]=\underline{0} \tag{3}$$

where $[\lambda_p]$ is the eigenvalue matrix ($\lambda_{pi}=\omega_{pi}^2$) and $\{\phi_{pi}\}$ are the eigenvectors (mode shapes). The pad's physical coordinate displacement vector $\{x_p\}$ is obtained from

$$\underset{(n\times 1)}{\{x_p\}}=\underset{(n\times m)}{[\phi_M]}\,\underset{(m\times 1)}{\{\xi_p\}}=\left[\underset{(n\times 1)}{\phi_{M1}}\,|\cdots|\,\underset{(n\times 1)}{\phi_{Mm}}\right]\underset{(m\times 1)}{\{\xi_p\}} \tag{4}$$

where m is the number of selected mode shapes, $[\phi_M]$ is the corresponding modal matrix, and $\{\xi_p\}$ is the modal coordinate vector. Substitution of Eq. (4) into Eq. (2) yields the reduced-order modal coordinate equations

$$\underset{(m\times n)}{[\phi_M]^T}\,\underset{(n\times n)}{[m_p]}\,\underset{(n\times m)}{[\phi_M]}\,\underset{(m\times 1)}{\{\ddot{\xi}_p\}}+\underset{(m\times n)}{[\phi_M]^T}\,\underset{(n\times n)}{[k_p]}\,\underset{(n\times m)}{[\phi_M]}\,\underset{(m\times 1)}{\{\xi_p\}}=\underset{(m\times n)}{[\phi_M]^T}\,\underset{(n\times 1)}{\{f_p\}} \tag{5}$$

Substituting the orthogonality relations

$$\underset{(m\times m)}{[M_p]}=\underset{(m\times n)}{[\phi_M]^T}\,\underset{(n\times n)}{[m_p]}\,\underset{(n\times m)}{[\phi_M]}=\begin{bmatrix}M_{p_1} & & 0\\ & \ddots & \\ 0 & & M_{p_m}\end{bmatrix} \tag{6}$$

$$\underset{(m\times m)}{[K_p]}=\underset{(m\times n)}{[\phi_M]^T}\,\underset{(n\times n)}{[k_p]}\,\underset{(n\times m)}{[\phi_M]}=\begin{bmatrix}K_{p_1} & & 0\\ & \ddots & \\ 0 & & K_{p_m}\end{bmatrix} \tag{7}$$

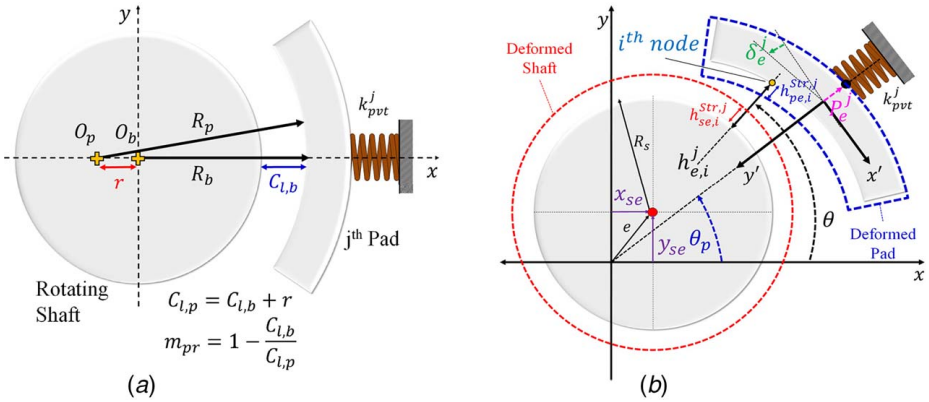

Fig. 4 Coordinates and parameters for the film thickness at the equilibrium state: (*a*) geometric parameters of the film thickness and (*b*) equilibrium position

Into Eq. (5) yields

$$\underset{(m\times m)}{[M_p]}\underset{(m\times 1)}{\{\ddot{\xi}_p\}}+\underset{(m\times m)}{[K_p]}\underset{(m\times 1)}{\{\xi_p\}}=\underset{(m\times 1)}{\{F_p\}} \tag{8}$$

which is utilized to obtain the dynamic coefficients including the effects of pad flexibility. The term $\{F_p\}$ is the modal force vector defined by

$$\underset{(m\times 1)}{\{F_p\}}=\underset{(m\times n)}{[\phi_M]^T}\underset{(n\times 1)}{\{f_p\}}=\begin{Bmatrix}F_{p_1}\\ \vdots\\ F_{p_m}\end{Bmatrix} \tag{9}$$

The calculation procedure for the bearing stiffness matrix components related to the journal and rigid pad modes ($\mathbf{k}_{JJ}$, $\mathbf{k}_{JR}$, $\mathbf{k}_{RJ}$, $\mathbf{k}_{RR}$) was provided in Ref. [52]. The stiffness matrices ($\mathbf{k}_{JF}$, $\mathbf{k}_{RF}$, $\mathbf{k}_{FF}$, $\mathbf{k}_{FR}$, $\mathbf{k}_{FJ}$) for the flexible pad's modal coordinates are provided below. The number of pads in the bearing is n_p. The magnitude of physical coordinate displacement and velocity perturbations was discussed in Ref. [52] for the rigid pad case. The modal coordinate displacement perturbation and modal coordinate velocity perturbation are given in Eqs. (10) and (11), respectively.

$$\Delta m^j_{k,pb}=\frac{0.01C_{l,b}}{\max\left(|\{\phi_{Mk,y'}\}|\right)} \tag{10}$$

$$\Delta \dot{m}^j_{k,pb}=\frac{0.01C_{l,b}\Omega_s}{\max\left(|\{\phi_{Mk,y'}\}|\right)} \tag{11}$$

The eigenvectors (mode shapes) are normalized by the maximum value $\max(|\{\phi_{Mk,y'}\}|)$ in the local coordinate y'-direction. The local y' coordinate is illustrated in Fig. 4(*b*). Thus, the scale of the modal displacement perturbations for the flexible modes is applied by Eq. (10), and the modal velocity perturbation is also taken by the multiplication of the modal displacement perturbations and operating speed as in Eq. (11). The kth eigenvector $\{\phi_{Mk,y'}\}$ includes only y-direction displacement in the local coordinate of a pad. The bearing stiffness matrix for the full set of rigid (R) and flexible (F) coordinates is

$$\left[k_{brg}\right]=\left[\begin{array}{c|c|c}\underset{(2\times 2)}{\mathbf{k}_{JJ}} & \underset{(2\times 2n_p)}{\mathbf{k}_{JR}} & \underset{(2\times mn_p)}{\mathbf{k}_{JF}}\\ \hline \underset{(2n_p\times 2)}{\mathbf{k}_{RJ}} & \underset{(2n_p\times 2n_p)}{\mathbf{k}_{RR}} & \underset{(2n_p\times mn_p)}{\mathbf{k}_{RF}}\\ \hline \underset{(mn_p\times 2)}{\mathbf{k}_{FJ}} & \underset{(mn_p\times 2n_p)}{\mathbf{k}_{FR}} & \underset{(mn_p\times mn_p)}{\mathbf{k}_{FF}}\end{array}\right]$$

$$=\left[\begin{array}{c|c|c|c|c|c|c}k_{xx} & k_{xy} & \mathbf{k}_{x\delta} & \mathbf{k}_{xp} & \mathbf{k}_{xm_1} & \cdots & \mathbf{k}_{xm_n}\\ \hline k_{yx} & k_{yy} & \mathbf{k}_{y\delta} & \mathbf{k}_{yp} & \mathbf{k}_{ym_1} & \cdots & \mathbf{k}_{ym_n}\\ \hline \mathbf{k}_{\delta x} & \mathbf{k}_{\delta y} & \mathbf{k}_{\delta\delta} & \mathbf{k}_{\delta p} & \mathbf{k}_{\delta m_1} & \cdots & \mathbf{k}_{\delta m_n}\\ \hline \mathbf{k}_{px} & \mathbf{k}_{py} & \mathbf{k}_{p\delta} & \mathbf{k}_{pp} & \mathbf{k}_{pm_1} & \cdots & \mathbf{k}_{pm_n}\\ \hline \mathbf{k}_{m_1x} & \mathbf{k}_{m_1y} & \mathbf{k}_{m_1\delta} & \mathbf{k}_{m_1p} & \mathbf{k}_{m_1m_1} & \cdots & \mathbf{k}_{m_1m_n}\\ \hline \vdots & \vdots & \vdots & \vdots & \vdots & \ddots & \vdots\\ \hline \mathbf{k}_{m_nx} & \mathbf{k}_{m_ny} & \mathbf{k}_{m_n\delta} & \mathbf{k}_{m_np} & \mathbf{k}_{m_nm_1} & \cdots & \mathbf{k}_{m_nm_n}\end{array}\right] \tag{12}$$

where

$$k_{m^i_k x}=-\frac{F^i_{p_k}(+\Delta x_{pb})-F^i_{p_k}(-\Delta x_{pb})}{2\Delta x_{pb}}, \tag{13}$$

(i, 1) term in $\mathbf{k}_{m_k x}$ $(n_p\times 1)$ in Eq. (12)

$$k_{m^i_k y}=-\frac{F^i_{p_k}(+\Delta y_{pb})-F^i_{p_k}(-\Delta y_{pb})}{2\Delta y_{pb}}, \tag{14}$$

(i, 1) term in $\mathbf{k}_{m_k y}$ $(n_p\times 1)$ in Eq. (12)

$$k_{m^i_k \delta^j}=-\frac{F^i_{p_k}(+\Delta\delta^j_{pb})-F^i_{p_k}(-\Delta\delta^j_{pb})}{2\Delta\delta^j_{pb}}, \tag{15}$$

(i, j) term in $\mathbf{k}_{m_k\delta}$ $(n_p\times n_p)$ in Eq. (12)

$$k_{m^i_k p^j}=-\frac{F^i_{p_k}(+\Delta p^j_{pb})-F^i_{p_k}(-\Delta p^j_{pb})}{2\Delta p^j_{pb}}, \tag{16}$$

(i, j) term in $\mathbf{k}_{m_k p}$ $(n_p\times n_p)$ in Eq. (12)

$$k_{x m^j_k}=-\frac{F_{s,x}(+\Delta m^j_{k,pb})-F_{s,x}(-\Delta m^j_{k,pb})}{2\Delta m^j_{k,pb}}, \tag{17}$$

(i, j) term in $\mathbf{k}_{xm_k}$ $(1\times n_p)$ in Eq. (12)

$$k_{y m^j_k}=-\frac{F_{s,y}(+\Delta m^j_{k,pb})-F_{s,y}(-\Delta m^j_{k,pb})}{2\Delta m^j_{k,pb}}, \tag{18}$$

(1, j) term in $\mathbf{k}_{ym_k}$ $(1\times n_p)$ in Eq. (12)

$$k_{\delta^i m^j_k}=-\frac{M^i_p(+\Delta m^j_{k,pb})-M^i_p(-\Delta m^j_{k,pb})}{2\Delta m^j_{k,pb}}, \tag{19}$$

(i, j) term in $\mathbf{k}_{\delta m_k}$ $(1\times n_p)$ in Eq. (12)

$$k_{p^i m^j_k}=-\frac{F^i_{pvt}(+\Delta m^j_{k,pb})-F^i_{pvt}(-\Delta m^j_{k,pb})}{2\Delta m^j_{k,pb}}, \tag{20}$$

(i, j) term in $\mathbf{k}_{pm_k}$ $(n_p\times n_p)$ in Eq. (12)

$$k_{m^i_k m^j_l}=-\frac{F^i_{p_k}(+\Delta m^j_{l,pb})-F^i_{p_k}(-\Delta m^j_{l,pb})}{2\Delta m^j_{l,pb}}+K^j_{P_k}, \tag{21}$$

$(i,\ j)$ term in $\mathbf{k}_{m_k m_l}$ $(n_p\times n_p)$ in Eq. (12)

The modal stiffness matrix in Eq. (7) is utilized in the modal stiffness term $k_{m^i_k m^j_l}$ of the full stiffness matrix in Eq. (12). This corresponds to perturbations of the modal coordinates. The components of the full damping matrix are obtained in a similar manner as with the full stiffness matrix.

$$\left[c_{brg}\right]=\left[\begin{array}{c|c|c}\underset{(2\times 2)}{\mathbf{c}_{JJ}} & \underset{(2\times 2n_p)}{\mathbf{c}_{JR}} & \underset{(2\times mn_p)}{\mathbf{c}_{JF}}\\ \hline \underset{(2n_p\times 2)}{\mathbf{c}_{RJ}} & \underset{(2n_p\times 2n_p)}{\mathbf{c}_{RR}} & \underset{(2n_p\times mn_p)}{\mathbf{c}_{RF}}\\ \hline \underset{(mn_p\times 2)}{\mathbf{c}_{FJ}} & \underset{(mn_p\times 2n_p)}{\mathbf{c}_{FR}} & \underset{(mn_p\times mn_p)}{\mathbf{c}_{FF}}\end{array}\right]$$

$$=\left[\begin{array}{c|c|c|c|c|c|c}c_{xx} & c_{xy} & \mathbf{c}_{x\delta} & \mathbf{c}_{xp} & \mathbf{c}_{xm_1} & \cdots & \mathbf{c}_{xm_n}\\ \hline c_{yx} & c_{yy} & \mathbf{c}_{y\delta} & \mathbf{c}_{yp} & \mathbf{c}_{ym_1} & \cdots & \mathbf{c}_{ym_n}\\ \hline \mathbf{c}_{\delta x} & \mathbf{c}_{\delta y} & \mathbf{c}_{\delta\delta} & \mathbf{c}_{\delta p} & \mathbf{c}_{\delta m_1} & \cdots & \mathbf{c}_{\delta m_n}\\ \hline \mathbf{c}_{px} & \mathbf{c}_{py} & \mathbf{c}_{p\delta} & \mathbf{c}_{pp} & \mathbf{c}_{pm_1} & \cdots & \mathbf{c}_{pm_n}\\ \hline \mathbf{c}_{m_1x} & \mathbf{c}_{m_1y} & \mathbf{c}_{m_1\delta} & \mathbf{c}_{m_1\delta} & \mathbf{c}_{m_1m_1} & \cdots & \mathbf{c}_{m_1m_n}\\ \hline \vdots & \vdots & \vdots & \vdots & \vdots & \ddots & \vdots\\ \hline \mathbf{c}_{m_nx} & \mathbf{c}_{m_ny} & \mathbf{c}_{m_n\delta} & \mathbf{c}_{m_n\delta} & \mathbf{c}_{m_nm_1} & \cdots & \mathbf{c}_{m_nm_n}\end{array}\right] \tag{22}$$

The full mass matrix of the total system consists of the journal's mass (m_s), the moment of inertia ($\mathbf{m}_{\delta\,\delta}$), rigid body pad mass ($\mathbf{m}_{pp}$), and modal mass of the pads ($\mathbf{m}_{m_k m_l}$) as in Eqs. (23)–(26).

$$\left[m_{brg}\right] = \begin{bmatrix} \underset{(2\times2)}{\mathbf{m}_{JJ}} & \underset{(2\times2n_p)}{\mathbf{m}_{JR}} & \underset{(2\times mn_p)}{\mathbf{m}_{JF}} \\ \underset{(2n_p\times2)}{\mathbf{m}_{RJ}} & \underset{(2n_p\times2n_p)}{\mathbf{m}_{RR}} & \underset{(2n_p\times mn_p)}{\mathbf{m}_{RF}} \\ \underset{(mn_p\times2)}{\mathbf{m}_{FJ}} & \underset{(mn_p\times2n_p)}{\mathbf{m}_{FR}} & \underset{(mn_p\times mn_p)}{\mathbf{m}_{FF}} \end{bmatrix} = \left[\begin{array}{c|c|c|c|c|c|c} m_s & 0 & 0 & 0 & 0 & \cdots & \mathbf{0} \\ \hline 0 & m_s & 0 & 0 & 0 & \cdots & 0 \\ \hline 0 & 0 & \mathbf{m}_{\delta\delta} & 0 & 0 & \cdots & 0 \\ \hline 0 & 0 & 0 & \mathbf{m}_{pp} & 0 & \cdots & 0 \\ \hline 0 & 0 & 0 & 0 & \mathbf{m}_{m_i m_l} & \cdots & 0 \\ \hline \vdots & \vdots & \vdots & \vdots & \vdots & \ddots & \vdots \\ \hline 0 & 0 & 0 & 0 & 0 & \cdots & \mathbf{m}_{m_n m_n} \end{array}\right] \tag{23}$$

$$m_{\delta^j\delta^j} = I_T^j, (j,j)\,\text{term in}\,\mathbf{m}_{\delta\delta}\,(n_p \times n_p)\,\text{in Eq. (12)} \tag{24}$$

$$m_{p^j p^j} = m_p^j, (j,j)\,\text{term in}\,\mathbf{m}_{pp}\,(n_p \times n_p)\,\text{in Eq. (12)} \tag{25}$$

$$m_{m_k^j m_l^j} = M_{P_k}^j, (j,j)\,\text{term in}\,\mathbf{m}_{m_k m_l}\,(mn_p \times mn_p)\,\text{in Eq. (12)} \tag{26}$$

The modal mass matrix of Eq. (6) is utilized in the modal mass term $m_{m_k^j m_l^j}$ of the full mass matrix in Eq. (23). This corresponds to perturbations of the modal coordinates.

The majority of rotordynamic modeling software packages require that the bearing matrices be 2×2, i.e., only relate the translational coordinates of the journal. This is also required in the rotordynamics simulations specified in the API standards for petrochemical plant rotating machinery acceptance [52]. The 2×2 matrices are obtained from the full dynamic coefficient matrices by imposing the condition that all degrees-of-freedom (journal, pads, pivots) vibrate at the same frequency (ν). This is referred to as frequency reduction, and the corresponding dynamic coefficients are referred to as "Frequency Reduced Dynamic Coefficients." The 2×2 matrix dynamic coefficients are obtained from Eqs. (27) and (28), and the necessary parameters are given in Eqs. (29)–(33). The specific derivation is described in the earlier study [52].

$$\underset{(2\times2)}{[\hat{k}_{JJ}]} = real\left(\underset{(2\times2)}{[Z'_{JJ}]}\right) \tag{27}$$

$$\underset{(2\times2)}{[\hat{c}_{JJ}]} = \frac{1}{\nu}\,imag\left(\underset{(2\times2)}{[Z'_{JJ}]}\right) \tag{28}$$

where

$$\underset{(2\times2)}{[Z'_{JJ}]} = \underset{(2\times2)}{[Z_{JJ}]} - \underset{2\times(2n_p+mn_p)}{[Z_{JP}]}\ \underset{\substack{(2n_p+mn_p)\\ \times(2n_p+mn_p)}}{[Z_{PP}^{-1}]}\ \underset{(2n_p+mn_p)\times2}{[Z_{PJ}]} \tag{29}$$

$$\underset{(2\times2)}{[Z_{JJ}]} = i\nu\,\underset{(2\times2)}{[c_{JJ}]} + \underset{(2\times2)}{[k_{JJ}]} \tag{30}$$

$$\underset{2\times(2n_p+mn_p)}{[Z_{JP}]} = i\nu\left[\underset{(2\times2n_p)}{\mathbf{c}_{JR}} \;\middle|\; \underset{(2\times mn_p)}{\mathbf{c}_{JF}}\right] + \left[\underset{(2\times2n_p)}{\mathbf{k}_{JR}} \;\middle|\; \underset{(2\times mn_p)}{\mathbf{k}_{JF}}\right] \tag{31}$$

$$\underset{(n_p+mn_p)\times2}{[Z_{PJ}]} = i\nu\begin{bmatrix} \underset{(n_p\times2)}{\mathbf{c}_{RJ}} \\ \hline \underset{(mn_p\times2)}{\mathbf{c}_{FJ}} \end{bmatrix} + \begin{bmatrix} \underset{(n_p\times2)}{\mathbf{k}_{RJ}} \\ \hline \underset{(mn_p\times2)}{\mathbf{k}_{FJ}} \end{bmatrix} \tag{32}$$

$$\underset{\substack{(2n_p+mn_p)\\ \times(2n_p+mn_p)}}{[Z_{PP}]} = i\nu\left[\begin{array}{c|c} \underset{(2n_p\times2n_p)}{\mathbf{c}_{RR}} & \underset{(2n_p\times mn_p)}{\mathbf{c}_{RF}} \\ \hline \underset{(mn_p\times2n_p)}{\mathbf{c}_{FR}} & \underset{(mn_p\times mn_p)}{\mathbf{c}_{FF}} \end{array}\right] + \left[\begin{array}{c|c} \underset{(2n_p\times2n_p)}{\mathbf{k}_{RR}} & \underset{(2n_p\times mn_p)}{\mathbf{k}_{RF}} \\ \hline \underset{(mn_p\times2n_p)}{\mathbf{k}_{FR}} & \underset{(mn_p\times mn_p)}{\mathbf{k}_{FF}} \end{array}\right] - \nu^2\left[\begin{array}{c|c} \underset{(2n_p\times2n_p)}{\mathbf{m}_{RR}} & \underset{(2n_p\times mn_p)}{\mathbf{m}_{RF}} \\ \hline \underset{(mn_p\times2n_p)}{\mathbf{m}_{FR}} & \underset{(mn_p\times mn_p)}{\mathbf{m}_{FF}} \end{array}\right] \tag{33}$$

Rotordynamic system studies combine the shaft, bearing, casing, seals, etc., sub-models into a total system model. The system model is utilized to determine free and forced vibration response characteristics such as natural frequencies, mode shapes, log decrements, imbalance response, etc. Modal log decrements quantify the damping present in the individual modes. Positive log decrements indicate stable, damped modes, a log decrement of zero indicates an undamped mode, and negative log decrements indicate unstable modes. The effect of changes of bearing parameters on log decrement is sometimes performed by considering a simplified rigid rotor model symmetrically supported on two identical TPJB [52]. The log decrements ($\delta_{dec,i}$) are determined from

$$\delta_{dec,i} = \frac{2\pi\varphi_i}{\sqrt{1-\varphi_i^2}} \tag{34}$$

where

$$\varphi_i = \frac{real(\lambda_{s,i})}{|\lambda_{s,i}|} \tag{35}$$

and $\lambda_{s,i}$ are system eigenvalues.

2.3 Boundary Conditions and Source Terms for Perturbation Forces (Computational Fluid Dynamics Solver). The CFD solver calculates the forces and moments resulting from the displacement perturbations and velocity perturbations, in order to determine the bearing stiffness and damping matrices. Perturbations of modal coordinates result in perturbations of the nodes on the pad surface via Eq. (4). This imparts displacement or velocity boundary motions on the fluid mesh in the CFD flow model. The pad structure's FEM mesh and the film's CFD mesh do not have identically located nodes. Therefore, motions and forces must be transferred via interpolation between the structural deformation and fluid meshes at the pad-film interface. The displacement perturbations of the pad surface mesh in the global x and y directions, as shown in Fig. 1, are determined from

$$\underset{(n_c/3\times1)}{\{\Delta x_{Fpb,k}^j\}} \overset{Interpolation}{\Leftarrow} \underset{(n/3\times1)}{\{\phi_{Mx,k}^j\}} \times \Delta m_{k,pb}^j \tag{36}$$

$$\underset{(n_c/3\times1)}{\{\Delta y_{Fpb,k}^j\}} \overset{Interpolation}{\Leftarrow} \underset{(n/3\times1)}{\{\phi_{My,k}^j\}} \times \Delta m_{k,pb}^j \tag{37}$$

The total number of pad j film surface nodes that connect the fluid film and pad is n_c in the CFD and n in the 3D structure, where n is 105, and n_c is determined from the 0.75 mm grid size of the hexahedron mesh. The terms $\{\phi_{Mx,k}^j\}$ and $\{\phi_{My,k}^j\}$ are x- and y-direction eigenvector components of the kth mode $\{\phi_{M,k}^j\}$ of pad j in Eq. (4). The modal coordinate displacement perturbation $\Delta m_{k,pb}^j$ of the kth mode of pad j is given in Eq. (10).

The values of the perturbed displacements are then substituted into Δx_{pb}, Δy_{pb}, Δp_{pb}^j, $\Delta\delta_{pb}^j$, $\Delta m_{k,pb}^j$ in Eqs. (38) and (39) to obtain:

Total perturbed displacements of the pad surface due to pad tilting, pivot motion, and multiple modes:

$$\Delta x^j_{p,i} = \underbrace{\left\{-\frac{\Delta\delta^j_{pb}}{R_s}x^j_{0,i}(y^j_{0,i}\cos\theta^j_p - x^j_{0,i}\sin\theta^j_p)\right\}}_{(\text{Tilting motion perturbation terms})} + \underbrace{\left\{\frac{\Delta p^j_{pb}}{R_s^2}x^j_{0,i}(x^j_{0,i}\cos\theta^j_p + y^j_{0,i}\sin\theta^j_p)\right\}}_{(\text{Pivot motion perturbation terms})} + \sum_{k=1}^{m}\underbrace{\left\{\frac{x^j_{0,i}}{R_s^2}(\Delta x^j_{Fpb,k,i}x^j_{0,i} + \Delta y^j_{Fpb,k,i}y^j_{0,i})\right\}}_{(\text{Perturbation terms from total } m \text{ modes})} \tag{38}$$

$$\Delta y^j_{p,i} = \underbrace{\left\{-\frac{\Delta\delta^j_{pb}}{R_s}y^j_{0,i}(y^j_{0,i}\cos\theta^j_p - x^j_{0,i}\sin\theta^j_p)\right\}}_{(\text{Tilting motion perturbation terms})} + \underbrace{\left\{\frac{\Delta p^j_{pb}}{R_s^2}y^j_{0,i}(x^j_{0,i}\cos\theta^j_p + y^j_{0,i}\sin\theta^j_p)\right\}}_{(\text{Pivot motion perturbation terms})} + \sum_{k=1}^{m}\underbrace{\left\{\frac{y_0}{R_s^2}(\Delta x^j_{Fpb,k,i}x^j_{0,i} + \Delta y^j_{Fpb,k,i}y^j_{0,i})\right\}}_{(\text{Perturbation terms from total } m \text{ modes})} \tag{39}$$

The derivation of the tilting and pivot motion perturbation terms are presented in the author's previous study [52], and the additional mode perturbation in the final term of Eqs. (38) and (39) are included to account for pad flexibility. The total perturbed displacements from Eqs. (38) and (39) are prescribed as boundary conditions for the fluid mesh deformation at the pad surfaces. The resulting force and moment changes are obtained from the pressure and shear stress distributions at the pad film surface for each perturbation. The results are saved and utilized to calculate the stiffness matrix.

The perturbed velocity terms are applied through the source terms of the mass conservation, momentum, and energy conservation equations for determining damping coefficients. The source terms are derived from the transient terms of the equations and can be written in terms of the film thickness as

Continuity equation with the perturbed velocity source term:

$$s^j_{C,i} = -\left(\frac{\partial\rho_f}{\partial t}\right)^j_i \simeq -\left(\frac{\rho_l}{h^j_{e,i}}\frac{\partial h^j_{e,i}}{\partial t}r_{l,i} + \frac{\rho_v}{h^j_{e,i}}\frac{\partial h^j_{e,i}}{\partial t}(1-r_{l,i})\right) \tag{40}$$

Momentum equation with the perturbed velocity source term:

$$s^j_{M,I,i} = -\left(\frac{\partial\rho_f u_I}{\partial t}\right)^j_i \simeq -\left(\frac{\rho_l u_I}{h^j_{e,i}}\frac{\partial h^j_{e,i}}{\partial t}r_{l,i} + \frac{\rho_v u_I}{h^j_{e,i}}\frac{\partial h^j_{e,i}}{\partial t}(1-r_{l,i})\right) \tag{41}$$

Energy equation with the perturbed velocity source term:

$$s^j_{E,i} = -\left(\frac{\partial\rho_f h^j_{tot}}{\partial t}\right)^j_i \simeq -\left(\frac{\rho_l C_{p,i}T_{f,i}}{h^j_{e,i}}\frac{\partial h^j_{e,i}}{\partial t}r_{l,i} + \frac{\rho_v C_{p,i}T_{f,i}}{h^j_e}\frac{\partial h^j_{e,i}}{\partial t}(1-r_{l,i})\right) \tag{42}$$

The equations represent the source terms for the ith element of pad j, and I-direction velocity. The source terms are functions of fluid properties, time derivatives of film thickness, film thickness at the equilibrium state, and dependent variables such as fluid volume fraction, velocity, and temperature.

The film thickness and its time derivative are required in the source terms (40)–(42). In order to calculate the film thickness at the equilibrium state [52], utilize

$$h^j_{e,i} = C_{l,p} - \frac{(C_{l,p}-C_{l,b})}{R_s}\{x^j_{0,i}\cos(\theta^j_p) + y^j_{0,i}\sin(\theta^j_p)\} - \frac{1}{R_s}\begin{bmatrix}\{x_{se}\,x^j_{0,i} + y_{se}\,y^j_{0,i}\}\\ -p^j_e\{\cos(\theta^j_p)x^j_{0,i} + \sin(\theta^j_p)y^j_{0,i}\}\\ +\delta^j_e R_s\{-\sin(\theta^j_p)x^j_{0,i} + \cos(\theta^j_p)y^j_{0,i}\}\end{bmatrix} - \{h^{Str,j}_{se,i} + h^{Str,j}_{pe,i}\} \tag{43}$$

The deformations of the shaft and pad by thermal and physical loads are given by

$$h^{Str,j}_{se,i} = \frac{1}{R_s}[\Delta x^{Str,j}_{se,i}x^j_{0,i} + \Delta y^{Str,j}_{se,i}y^j_{0,i}] \tag{44}$$

$$h^{Str,j}_{pe,i} = \frac{1}{R_s}[\Delta x^{Str,j}_{pe,i}\,x^j_{0,i} + \Delta y^{Str,j}_{pe,i}\,y^j_{0,i}] \tag{45}$$

The superscript j indicates the pad number, the subscript i indicates the element number, and the subscript 0 indicates the initial nodal location. All element location values x, y, z in Eq. (43) are expressed in the global x, y, and z coordinates. The equilibrium configuration is obtained from the statics solution, and the equilibrium positions of all degrees-of-freedom and the relevant geometric parameter are illustrated in Fig. 4.

The fim thickness time derivative terms in Eqs. (40)–(42) are affected by pertubations of the time derivatives of the bearing's rigid and flexible degrees-of-freedom $\Delta\dot{x}_{pb}$, $\Delta\dot{y}_{pb}$, $\Delta\dot{p}^j_{pb}$, $\Delta\dot{\delta}^j_{pb}$, $\Delta\dot{m}^j_{k,pb}$. This is shown explicitly by the following equations

$$\frac{\partial h^j_{e,i}}{\partial t} = -\frac{1}{R_s}\begin{bmatrix}\underbrace{\{\Delta\dot{x}_{pb}x^j_{0,i} + \Delta\dot{y}_{pb}y^j_{0,i}\}}_{(\text{shaft translational motion velocity perturbation terms})}\\ \underbrace{-\Delta\dot{p}^j_{pb}\{\cos(\theta^j_p)x^j_{0,i} + \sin(\theta^j_p)y^j_{0,i}\}}_{(\text{Pivot motion velocity perturbation terms})}\\ \underbrace{+\Delta\dot{\delta}^j_{pb}R_s\{-\sin(\theta^j_p)x^j_{0,i} + \cos(\theta^j_p)y^j_{0,i}\}}_{(\text{Tilting motion velocity perturbation terms})}\\ +\sum_{k=1}^{m}\underbrace{\{\Delta\dot{x}^j_{Fpb,k,i}x^j_{0,i} + \Delta\dot{y}^j_{Fpb,k,i}y^j_{0,i}\}}_{(k^{th}\text{ mode velocity perturbation terms})}\end{bmatrix} \tag{46}$$

$$\underbrace{\{\Delta\dot{x}^j_{Fpb,k}\}}_{(n_c/3\times1)} \overset{Interpolation}{\Leftarrow} \underbrace{\{\phi^j_{Mx,k}\}}_{(n/3\times1)} \times\Delta\dot{m}^j_{k,pb} \tag{47}$$

$$\underbrace{\{\Delta\dot{y}^j_{Fpb,k}\}}_{(n_c/3\times1)} \overset{Interpolation}{\Leftarrow} \underbrace{\{\phi^j_{My,k}\}}_{(n/3\times1)} \times\Delta\dot{m}^j_{k,pb} \tag{48}$$

The kth flexible pad modal coordinate's perturbation $\Delta\dot{m}^j_{k,pb}$ of pad j is implicitly included in Eq. (46) via the x and y direction displacements $\Delta\dot{x}^j_{Fpb,k,i}$, $\Delta\dot{y}^j_{Fpb,k,i}$, as shown by Eqs. (47) and (48). The modal coordinate velocity perturbation $\Delta\dot{m}^j_{k,pb}$ for the kth mode of pad j is defined in Eq. (11). Equation (46) is derived from the film thickness model after changing θ coordinate to x–y coordinate. The film thickness time derivative is substituted into the source terms (40)–(42) for each perturbation in order, while maintaining the equilibrium film thickness obtained from the static calculation. The perturbed force results are saved for each velocity perturbation, and they are then utilized to calculate the damping coefficients, similarly with the stiffness coefficient procedure.

2.4 Calculation Procedure. The approach to use CFD for the static analysis of rigid pad TPJB is presented in Ref. [51] and is also employed in this study. The calculation process for obtaining TPJB

dynamic coefficients, including pad flexibility effects, utilizes MATLAB coding, PYTHON coding, and a commercial CFD solver during each perturbation computation. As illustrated in Fig. 5, the MATLAB code calculates and assembles the stiffness and mass matrix of the pads and determines the eigenvectors. This code also interpolates perturbation generated pressure and shear stress distributions at the pad surface from the CFD model into equivalent, 3D structure, and nodal forces. Finally, the MATLAB code utilizes these forces to determine the modal forces in the structural model, in order to generate the full bearing dynamic coefficient matrices. These coefficients are, in turn, used to calculate the frequency reduce dynamic coefficients of the TPJB. The primary role of the CFD solver is to determine the perturbed forces resulting from the modal-based displacement and velocity perturbations. Each perturbation is controlled by the Job script based on the PYTHON code.

2.5 Selection of Flexible Pad Modes for Dynamic Coefficients. Selecting a minimal set of dominant flexible pad modes can provide a significant reduction in computational time when including pad flexibility effects in the calculation of dynamic coefficients. This may be accomplished by considering the effects of the modes on dynamic coefficient for representative parameter sets, as shown in Table 3. The Reynolds film model is utilized in this study to economize on computation time. Mode shapes may be classified according to distinguishing geometric features, as illustrated in Fig. 6. Class A modes have symmetry about both the x–y and y–z planes. Class B modes are symmetric only about the x–y plane. Class C modes lack symmetry about either plane. Figure 6 shows the lowest mode in each class and corresponds to the nominal parameter set in Table 3.

The minimal set of dominant modes for this example is identified via inspection of the dynamic coefficient for all combinations of the modes in Fig. 6, according to class.

The lowest 20 modes are searched to determine the dominant modes for evaluating the dynamic coefficient, including pad flexibility effects. The selection of 20 as the appropriate number of retained modes is based on balancing accuracy and computation time [31], when considering eccentricity ratio, attitude angle, film thickness, stiffness, and damping. Pivot stiffness and pad thermal deformation are neglected in the search to focus primarily on pad flexibility effects. The pivot type is still considered, though, in terms of the boundary condition, it exerts on the pad's 3D model. The boundary condition is either fixed along a line (cylindrical pivot) or at a point (spherical pivot). The calculation procedure for comparing the dynamic coefficient results for the full 20 mode case versus the reduced mode (m) cases is illustrated in Fig. 7. The best mode combination with the minimum error is extracted for the selected m mode case. The error is defined by the relative difference between the direct dynamic coefficients with 20 modes versus the selected m modes.

The best mode number combinations are presented as cases 1–9 in Table 4. The error relative to the full 20 mode simulation is less than 0.5% for all cases, and over all frequency reduced stiffness and damping coefficients. This study shows that flexible mode numbers 2–5 have the greatest effect on accuracy, the first bending mode is the dominant mode shape, and the shape of the class A modes produce the most significant perturbation modal forces. The significance of the class A and B modes is comparable for the case of 0.6 offsets (Case 8). Summarizing for this example, utilizing 4 or 5 modes from Class A and Class B is sufficient for determining the dynamic coefficients including pad flexibility.

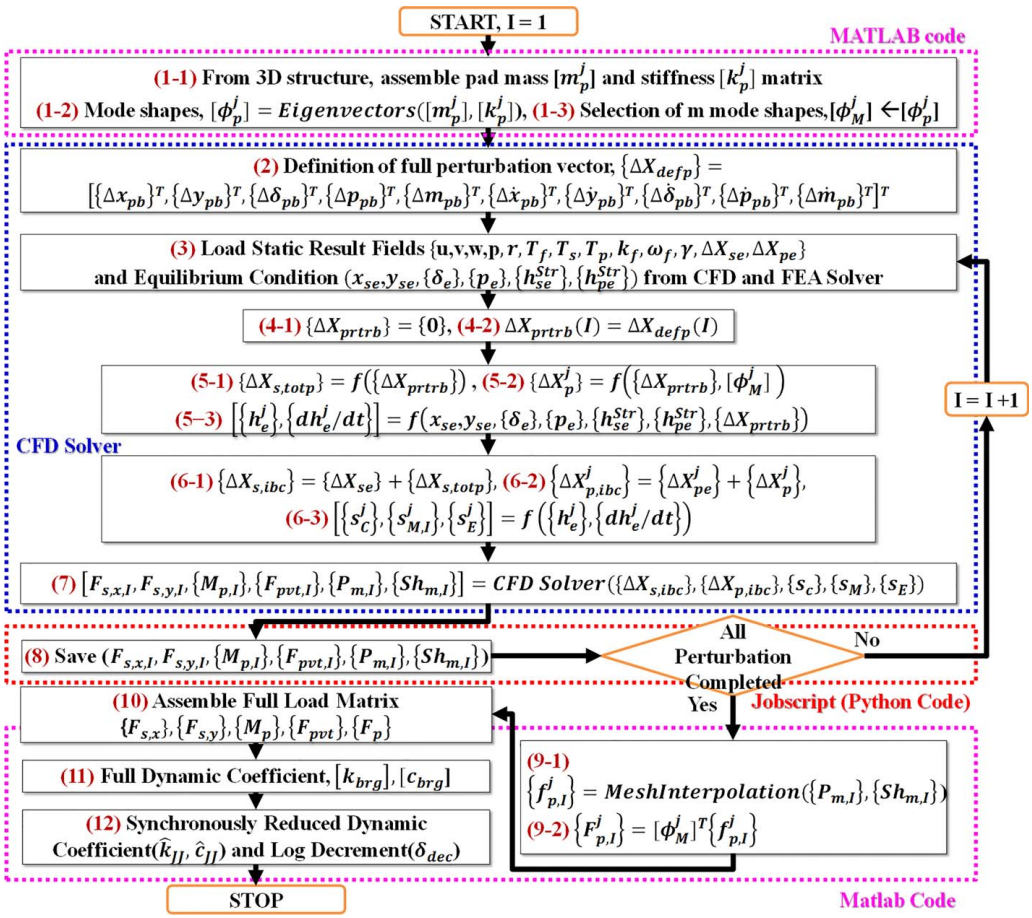

Fig. 5 Procedure for calculating dynamic coefficients including multi-mode pad flexibility

Table 3 Case studies for dominant mode identification

Input parameters	N	Case 1	Case 2	Case 3	Case 4	Case 5	Case 6	Case 7	Case 8	Case 9
Shaft radius (mm)	50.8	76.2	50.8	50.8	50.8	50.8	50.8	50.8	50.8	50.8
Bearing length (mm)	50.8	50.8	101.6	50.8	50.8	50.8	50.8	50.8	50.8	50.8
Bearing clearance (um)	74.9	112	74.9	60	74.9	74.9	74.9	74.9	74.9	74.9
Pad arc length (deg)	60	60	60	60	56	60	60	60	60	60
Pad thickness (mm)	12.7	19.1	12.7	12.7	12.7	19.1	12.7	12.7	12.7	12.7
Rotating speed (krpm)	15	15	15	15	15	15	3	15	15	15
Applied load (kN)	5	5	5	5	5	5	5	10	5	5
Offset	0.5	0.5	0.5	0.5	0.5	0.5	0.5	0.5	0.6	0.5
Pivot type	Cyn.	Cyn.	Cyn.	Cyn.	Cyn.	Cyn.	Cyn.	Cyn.	Cyn.	Sph.

Note: N: nominal case; Cyn.: cylindrical type pivot; and Sph.: spherical-type pivot.

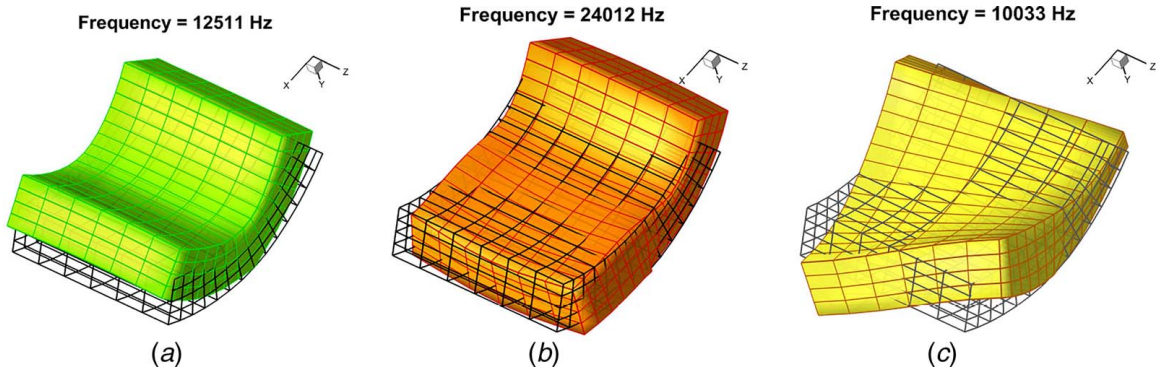

Fig. 6 Classification of pad mode shapes: (*a*) Class A: *x–y* and *y–z* symmetry, (*b*) Class B: *x–y* symmetry, and (*c*) Class C: non-symmetric

3 Results Comparison of the Reynolds Versus Computational Fluid Dynamics Models With Pad Flexibility

This section presents a comparison between TEHD, CFD, and TEHD Reynolds models, including pad flexibility effects. The models include leading-edge film temperatures that are prescribed (without mixing), and those that result from mixing of supply and carryover flows between pads, in the operating speed range from 3000 to 15,000 rpm [51]. The pad inlet (leading edge) and outlet (trailing edge) boundaries are prescribed with constant temperature (40 °C) and pressure (132 kPa) for the "without Mixing" conditions. The CFD and Reynolds models compare closely for the prescribed leading edge (without mixing) film temperature case. This validates the CFD model, which has expected results very similar to the Reynolds model in the thin-film regime, given the same boundary conditions [51]. The next step was to compare the approaches, including mixing between pads and pad flexibility (which was ignored in Ref. [51]). The actual BP geometry with 3D thermal flow is included in the "with Mixing" condition of CFD approach. The Reynolds model employs the MC with 0.4 and 1.0 extremes in the "with Mixing" condition [51].

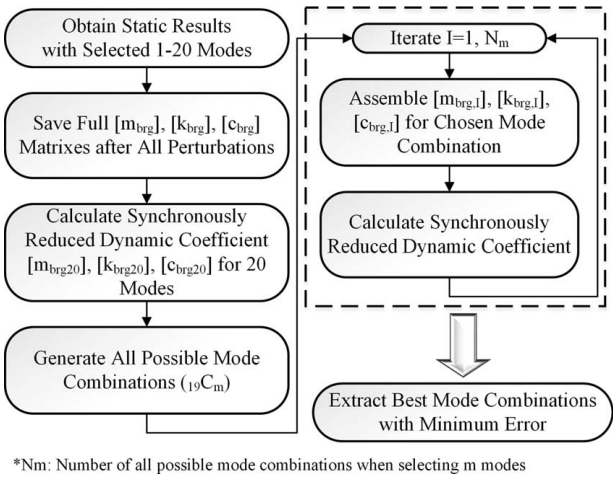

Fig. 7 Calculation procedure for determining best mode combinations

The input parameters are given in Table 5, along with the thermal boundary condition of a convection heat transfer coefficient of 50 W/m^2 and ambient temperature of 30 °C applied on the shaft and pad outer surfaces. The class A type modes (Numbers 3, 8, 10, 15) are employed in the flexible pad, CFD simulation, as explained in Sec. 2.5. The CFD model employs 451,834 elements, which is discussed in the grid study of the author's prior paper [51]. Also, the Jeffcott rotor mass for determining log decrements is 1019 kg. The lubricant is ISO-32, and the viscosity-temperature relation is an Andrade curve fit from two measured viscosity-temperature pairs, i.e, a 40 °C reference temperature (T_{ref}) and 100 °C second temperature.

In Part I, the entire (full) bearing model is simulated, including all pads, BPs, journal, film, etc. For the case when pad flexibility is included, the TEHD Reynolds and CFD model requires 1.07 h and 69 h wall clock times, respectively. The Reynolds model utilizes a single core of Intel Xeon CPU E5-1650 v4 3.6 GHz, and the CFD takes advantage of 12 cores of a computer server based on the dual Intel Xeon 2.5 GHz E5-2670 v2 (TAMU High Performance Research Computing Center HPRC). Part II utilizes a training set consisting of 1000s of different parameter value sets for use with the machine learning algorithm. The full bearing is not included in the training set CFD, which would be computationally impractical. Instead, the model is limited to the BP region in order to utilize CFD to determine MCs for the Reynolds model. These runs are made with up to 40 cases executing in parallel to reduce overall

Table 4 Best mode combinations with below 0.5% error and the mode classifications

		Best mode number combinations				Full modes, 1–20 (U)		
		Class				Class		
Case No.	Flexible mode No. m	A	B	C	Error (%)	A	B	C
N	3	3* 10 15	×	×	0.37	3* 8 10 15 18 19 20	7 14 16	U—(A + B)
1	2	4* 8	×	×	0.42	4* 8 11 14	7 10 15 17 18	
2	2	3* 15	×	×	0.44	3* 12 15 17 20	5 7 9 10 18	
3	4	3* 8 10 15	×	×	0.40	3* 8 10 15 18 19 20	7 14 16	
4	3	3* 10 15	×	×	0.17	3* 8 10 15 17 19 20	7 9 14 16	
5	3	4* 8 14	×	×	0.29	4* 8 10 14 17 19	7 12 15 16 20	
6	2	3* 10	×	×	0.49	3* 8 10 15 18 19 20	7 14 16	
7	4	3* 8 10 15	×	×	0.20	3* 8 10 15 18 19 20	7 14 16	
8	5	4* 9	7 8 17	×	0.22	4 9 14 16 19 20	7 8 11 15 17	
9	3	4* 8 10	×	×	0.33	4 8 10 14 17 19 20	6 11 15 16	

Note: *First bending mode; N: nominal case.

Table 5 Input parameters for CFD simulation model

Parameters	Value	Parameters	Value
Shaft diameter (mm)	101.6	**Fluid property, ISO 32**	
Bearing length (mm)	50.8	Liquid density (kg/m^3)	860
Bearing clearance (mm)	0.0749	Liquid viscosity (Pa s)	$0.03424e^{-0.0304(T_f - T_{ref})}$
Number of pads	5	Liquid specific heat (J/kg °C)	2000
Pad thickness (mm)	12.7	Liquid heat conductivity (W/mK)	0.133
Pad offset	0.5	Vapor density (kg/m^3)	0.029
Pad arc length (deg)	60	Vapor viscosity (Pa s)	9e-6
BP height (mm)	5.2	Vapor specific heat (J/kg°C)	1000
BP nozzle hydraulic diameter (mm)	1.8	Vapor heat conductivity (W/mK)	0.026
BP seal radial clearance (mm)	0.425	Cavitation pressure (kPa g)	−90
Applied load (N)	5000	**Solid property, steel (pad, shaft, and pivot)**	
Preload	0.5	Density (kg/m^3)	7850
Operating speed (krpm)	3–15	Specific heat (J/kg°C)	434
Supply pressure (kPa)	132	Heat conductivity (J/m°C)	60.5
Pivot configuration (cylindrical pivot)		Young's modulus (GPa)	210
Circumferential radius (pivot), (mm)	62	Poisson's ratio	0.29
Axial radius (pivot), (mm)	1270	Thermal expansion coefficient (1/°C)	1.1×10^{-5}
Circumferential radius (housing) (mm)	−69.7	Zero strain reference temperature (°C)	35
Axial radius (housing) (mm)	∞		

wall clock time. The between pad BP only model introduces some approximations that are explained in Part II.

Static response results and dynamic response results are presented in Figs. 8–10, respectively, for the "with pad flexibility" model. The static and dynamic results show excellent agreement between the Reynolds model and the CFD model for the "without Mixing" condition case. This supports the validity of the CFD approach for the pad region and for the pad flexibility model. The "without Mixing" condition results are very insensitive to pad flexibility, except for stiffness and damping in Figs. 9(*a*) and 9(*b*) and Figs. 10(*a*) and 10(*b*). This is consistent with past studies [6,11,31,23,34] showing that pad flexibility lowers damping and also affects stiffness.

In contrast to the "without Mixing" results, pad flexibility has a more significant effect in the "with mixing" results, especially at higher speeds. The eccentricity ratio in the CFD model is seen to increase (+20.6% at 15 krpm) when pad flexibility is included in the "with mixing" (BP) case, as shown in Fig. 8(*a-2*). A plausible explanation for this is that the pressure on the pad surface deforms the bottom pad, and this results in a slight lowering of the journal.

Figures 9 and 10 show −16.4% and −16.6% decreases in the synchronously reduced (Sec. 2.2) *x*-direction direct stiffness and *x*-direction direct damping, respectively, when pad flexibility is included in the CFD model. The *y*-direction damping and stiffness show similar reductions in the CFD model when pad flexibility is included. The comparable decrease of the stiffness and damping coefficients causes a reduction of the log decrement, as shown in Figs. 9(*c-2*) and 10(*c-2*), which implies the possible reduction of the rotor-bearing system stability margin.

The sensitivity of the Reynolds results to the MC is significant, except for eccentricity ratio, which shows increased sensitivity with speed. This result shows similar trends with that reported in the earlier study [51,52]. Some Reynolds results (eccentricity ratio, stiffness coefficient, damping coefficient, and log decrement) show a disparity with the CFD model for all values of the MC. Some CFD results (peak pad temperature and shaft average temperature) fall within the Reynolds result bounds (MC equals 0.4 and 1.0); however, the MC needed to make the two approaches agree differs depending on the result considered and the operating speed. This MC value is near 1.0 for shaft average temperature, for rpm <9,000, but MC in the range (0.4–1.0) cannot match results at higher rpm.

The CFD and Reynolds models were in close agreement without mixing because the CFD pad inlet temperature distributions were imposed to be uniform in the axial and radial directions. The higher fidelity CFD model, including between pad thermal-flow effects, yields pad inlet temperature distributions that are nonuniform at the pad inlets. This causes significant localized thermal heat flow into the shaft at the leading edge. This phenomenon is

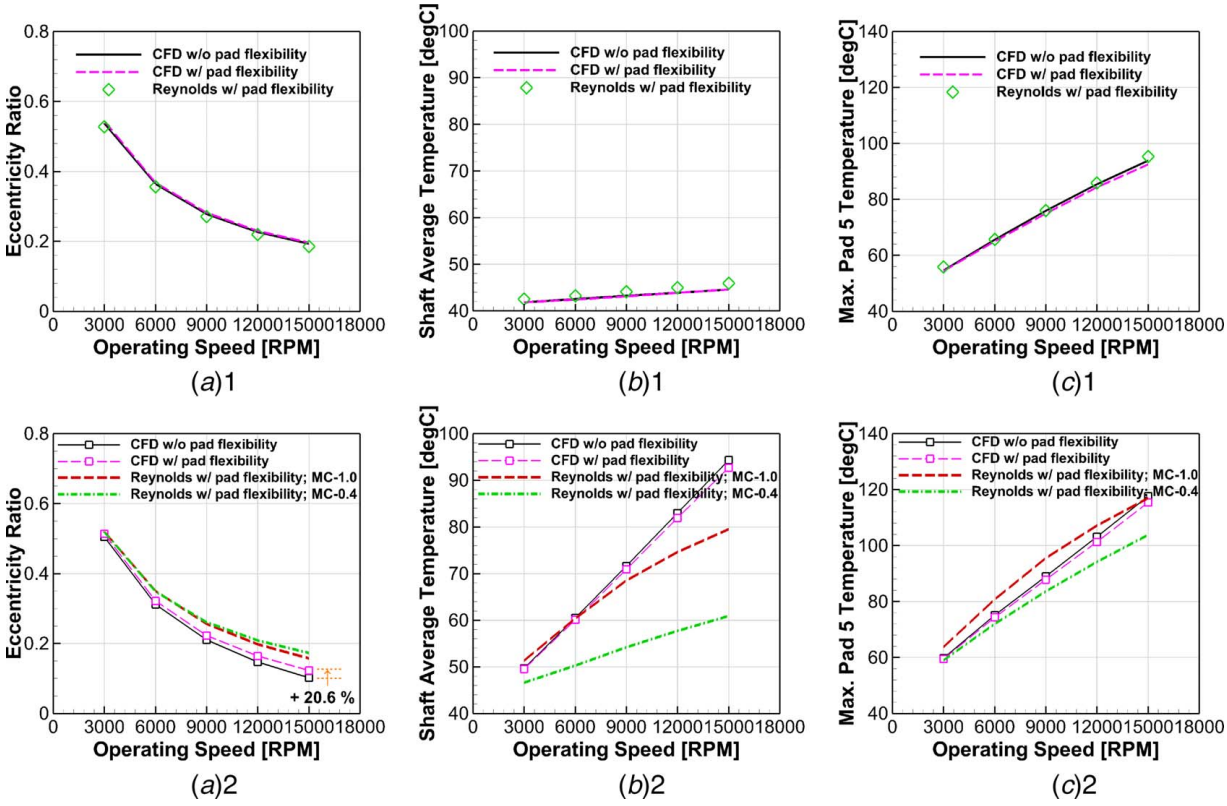

Fig. 8 Comparison of static performance with and w/o pad flexibility and w/o (1) and with (2) mixing: (*a*) eccentricity ratio, (*b*) shaft average temperature, and (c) max. pad 5 temperature.

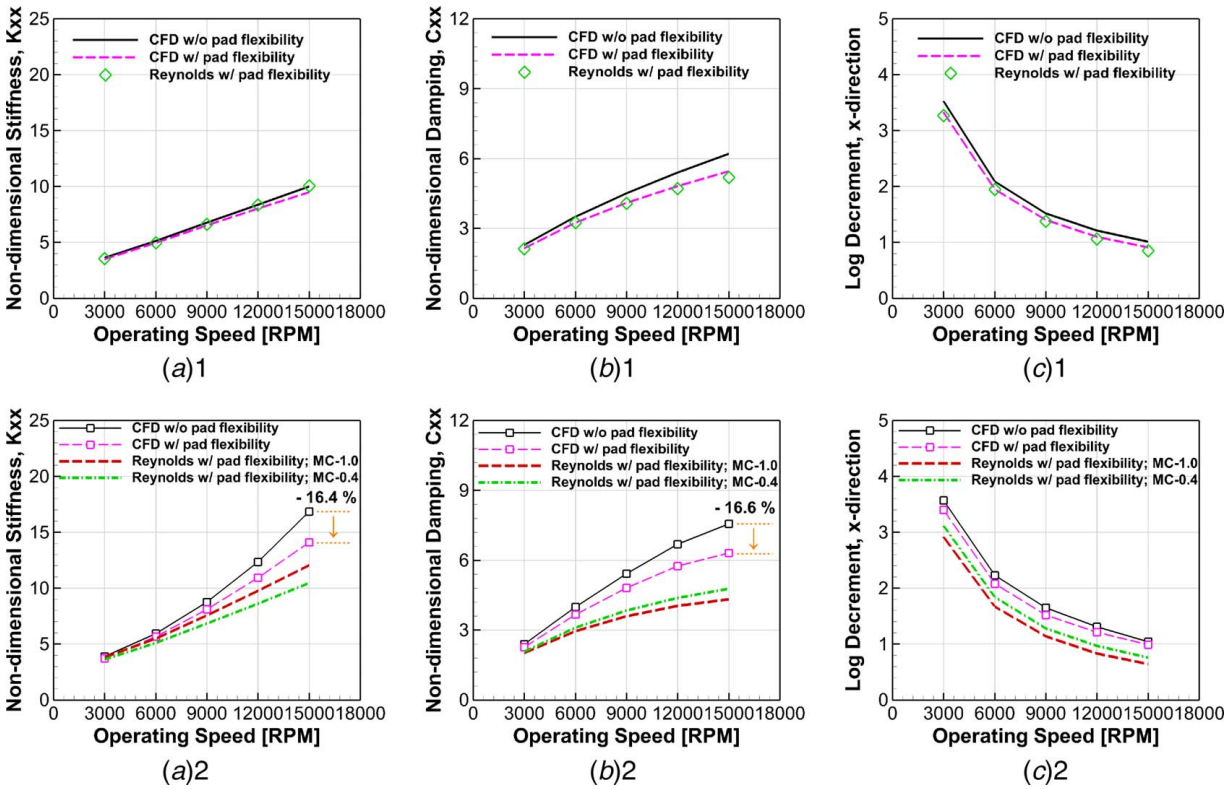

Fig. 9 Comparison of dynamics results with pad flexibility w/o (1) and with (2) mixing: (*a*) X stiffness Kxx, (*b*) X damping Cxx, and (c) X log decrement

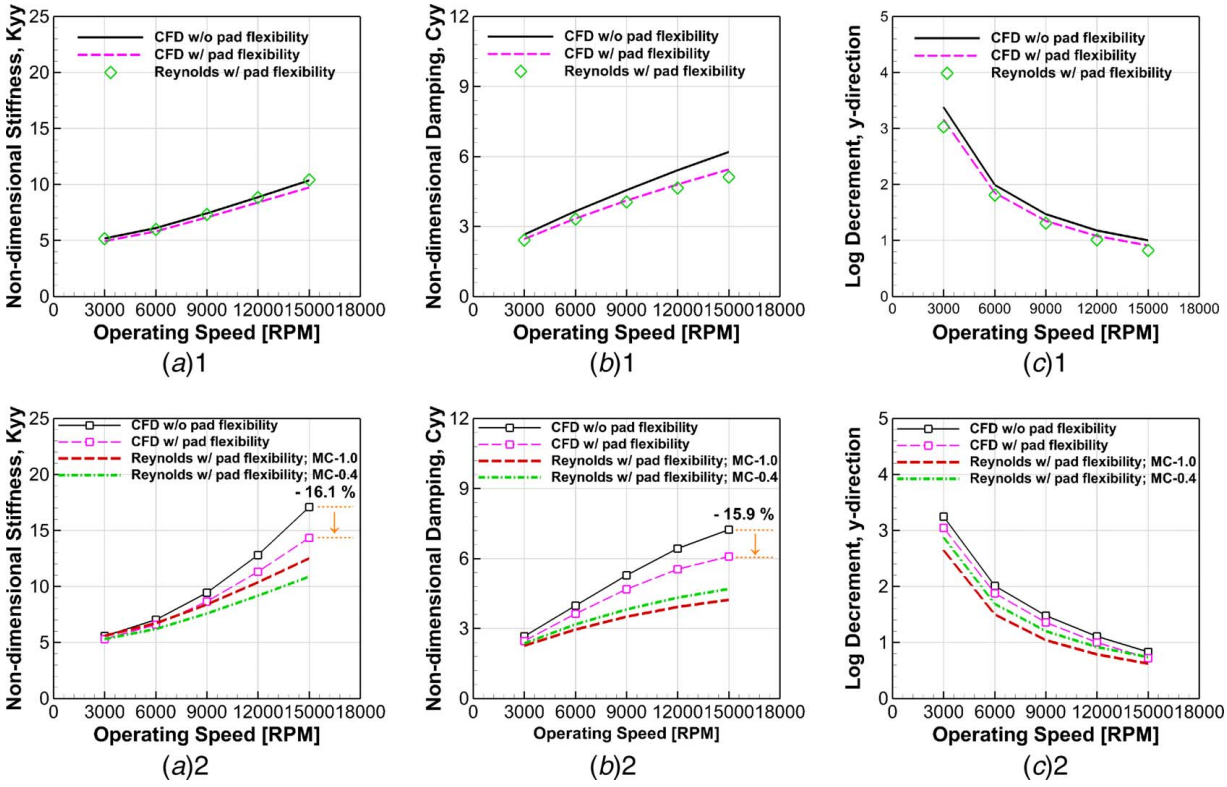

Fig. 10 Comparison of dynamics results with pad flexibility w/o (1) and with (2) Mixing: (*a*) Y stiffness Kyy, (*b*) Y damping Cyy, and (*c*) Y log decrement

not represented in the Reynolds model for any value of MC, since the Reynolds model assumes uniform inlet temperature distributions. Consequently, the CFD results do not need to fall within the bounds of the Reynolds model for MC—0.4 and 1.0.

4 Comparison With Experimental Results

The TEHD CFD model with pad flexibility effect was validated by comparison of predictions with the experimental results of Carter [53] and Kulhanek [54]. The TPJB in their test rig is shown in Fig. 11, and the researchers employed the same Leading Edge Groove (LEG) TPJB. Carter [53] tested a 0.6 pad offset bearing, and Kulhanek [54] tested both 0.5 and 0.6 pad offset cases. The 0.5 pad offset cases are compared with Kulhanek [54]. The 0.6 pad offset cases are compared with a blend of Carter [53] and Kulhanek [54] test results, as explained here. The pad temperature is compared with Carter [53], since temperature measurements are not provided in Kulhanek [54]. The eccentricity ratio and dynamic coefficients are compared with Kulhanek [54] because of its improved measurement probes. Carter [53] results are also utilized for estimating some uncertain magnitudes.

Suh and Palazzolo [31] also correlated their theoretical work (TEHD Reynolds) with the 0.5 pad offset measurements of Kulhanek [54]. However, the pivot stiffness was unknown and assumed to be similar to one in a different test rig. In addition, the convective heat transfer coefficients of the shaft and pad outer surfaces were underestimated. The present simulation model utilizes the manufactured pivot configuration, and the material properties and heat convection on the pad and shaft surfaces are evaluated approximately from the CFD simulation.

Input parameters are shown in Table 6 for the two offset cases, 0.5 and 0.6. Each case has a load between pad (LBP) of 6337 N (1034 kPa) and 10559 N (1723 kPa). The load and rotation directions are shown in Figs. 11(*a*) and 11(*b*). Total pressure at the oil supply inlet is obtained from the measured static pressure and supply oil flowrate, as shown in Table 7 and is prescribed at the oil supply inlet in the CFD model. A 150 kPa static pressure is applied at the trailing and leading edges for all cases with the Reynolds model. All other input parameters and boundary conditions are identical to those in Ref. [51]. The measurement uncertainty of the stiffness and damping was reported to be relatively small with a maximum of about 13% and generally less than 5%.

Figures 12 and 13 show static result comparisons with test, CFD, and Reynolds predictions. Figures 12(*a-1*) and 12(*a-2*) show good agreement between test and CFD, and poor between test and Reynolds for the oil supply flowrate prediction. The latter result is due to the inability of the Reynolds approach to model BP flow. The CFD results slightly over-predict the supply flowrate, since it does not consider full oil flow downstream of the bearing, but the error is small. The supply flowrate is similar for both load conditions.

Figure 12(*b*) shows eccentricity ratio results, and the CFD and Reynolds models show good agreement with the test results for both load conditions. CFD provides better agreement with test than Reynolds in the 0.5 offset case. Reynolds, with MC-0.4, shows better agreement with test than the CFD in the 0.6 offset case. However, this selection of the MC yields a larger discrepancy with test than CFD, for the pad 4 temperature prediction in Fig. 13(*b*). Thus, optimizing the Reynolds model with respect to MC selection is unreliable if only a single output is considered, and therefore, CFD provides a more dependable approach.

Figure 13 compares measured and predicted pad temperatures. Figure 13(*a*) shows excellent agreement between test, Reynolds, and CFD for upper pad temperature (Pad 1) with 1034 and 1723 kPa loads. Figure 13(*b*) provides a clear example of how uncertainty in the MC can yield highly inaccurate predictions from the Reynolds approach, while the CFD maintains very good agreement with the test results. The divergence between CFD and test at high speeds and 1723 kPa load results from the measured attitude angle being larger than the CFD predicted one. The larger attitude angle increases the pad 5 temperature while decreasing the pad 4 temperature. However, even in this case, the errors between theory and experiment are small.

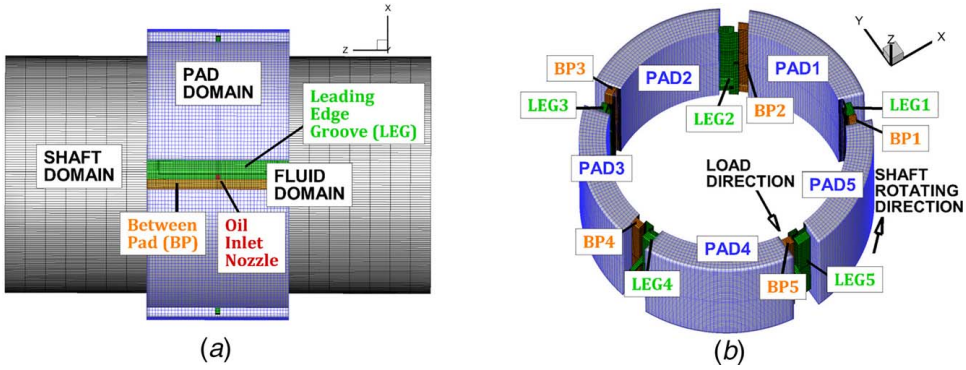

Fig. 11 Computational domain for a LEG TPJB in Carter [53] and Kulhanek [54]: (*a*) cross-sectional view and (*b*) TPJB overview

Table 6 Input parameters of LEG TPJB CFD simulation

Parameters	Value	
	0.5 Offset [54]	0.6 Offset [53], [54]
Shaft diameter (mm)	101.587	
Bearing length (mm)	60.325	
Bearing clearance (mm)	0.0814	0.0792
Number of pads	5	
Pad thickness (mm)	11.5	
Pad thickness at pivot (mm)	18.5	
Pad arc length (deg)	57.87	
Applied load (N)	(1) 6337 (2) 10,559	
Preload	0.273	0.283
Operating speed (krpm)	7–16	4–13
Pivot type	Rocker (Cylindrical)	
Load type	LBP	
Lubricant	ISO 32 [54]	
Outside HC (W/m^2K)	(1) 1500 (Pad) (2) 250 (Shaft)	
Ambient temperature (C)	(1) 43.3 (Pad) (2) 20 (Shaft)	
Supply oil temperature (C)	43.3	
Selected pad flexible modes	4,10,20	4,7,9
Solid property, steel		
Density (kg/m^3)	7850	
Heat conductivity (J/m °C)	42.6	
Young's modulus (GPa)	200	
Poisson's ratio	0.29	
Thermal expansion coef. (1/°C)	1.0e–5	
Reference temperature (°C)	43.3	

Note: HC: heat transfer coefficient.

Figures 14 and 15 compare measured and predicted non-dimensional, synchronously reduced dynamic coefficients, in the *x* and *y* directions, respectively. Figure 14(*a-1*) shows slightly better agreement between Reynolds and test, than the CFD and test, for the 0.5 offset case stiffness Kxx. Figures 14(*a-2*), 14(*b-1*), and 14(*b-2*) show much better agreement between CFD and test, compared with Reynolds and test, for stiffness Kxx (offset = 0.6) and damping Cxx (offsets = 0.5, 0.6), for both load cases. The *y*-direction stiffness Kyy and damping Cyy are also more accurately predicted with the CFD approach, as compared with the Reynolds approach, for all offset and load conditions, as shown in Fig. 15.

Kulhanek [54] and Carter [53] utilized the same test rig. However, Kulhanek [54] reported that his use of modified probe locations prevented the over-prediction of dynamic coefficient in Carter [53] due to excessive housing flexibility. Figure 15(*a-2*) and 15(*b-2*) show that Carter [53] measurements are considerable larger than Kulhanek [54] in all 0.6 offset results. The CFD results are consistent with Kulhanek [54].

This correlation study showed very good agreement between the CFD-TEHD approach and test for all cases, and generally good agreement between the Reynolds-TEHD approach and test. An exception was damping for the 0.5 offset case where the Reynolds-TEHD approach performed poorly. The superiority of the CFD over the Reynolds approach was confirmed in most of the results. Notably, the negative effect of MC uncertainty on Reynolds results was especially acute for pad temperature prediction.

All CFD and Reynolds model results in this section included pad flexibility effect. Table 8 shows the dynamic coefficient percent

Table 7 Total pressure at supply oil inlet

Operating speed (rpm)		4000	7000	10000	13,000	16,000
Total pressure (kPa)	0.5 Offset (6337 N)	–	262	286	526	787
	0.5 Offset (10,559 N)	–	273	284	530	791
	0.6 Offset (6337 N)	246	310	284	469	–
	0.6 Offset (10,559 N)	255	310	290	451	–

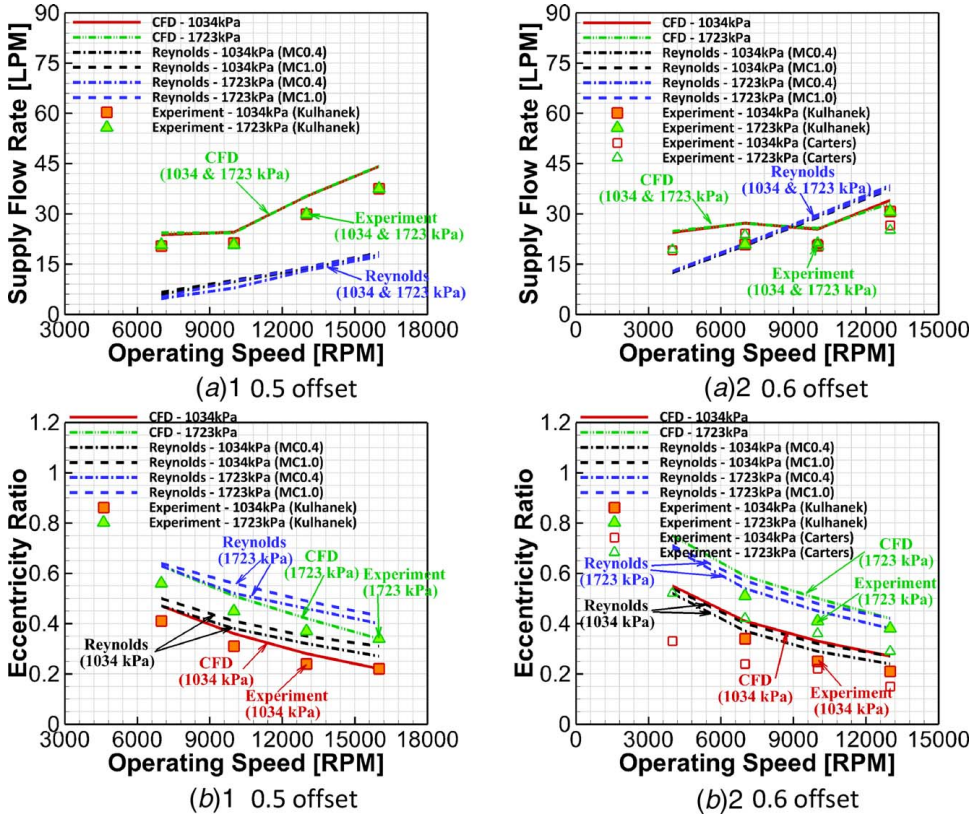

Fig. 12 Static results comparison (1): (*a*) supply flowrate and (*b*) eccentricity ratio

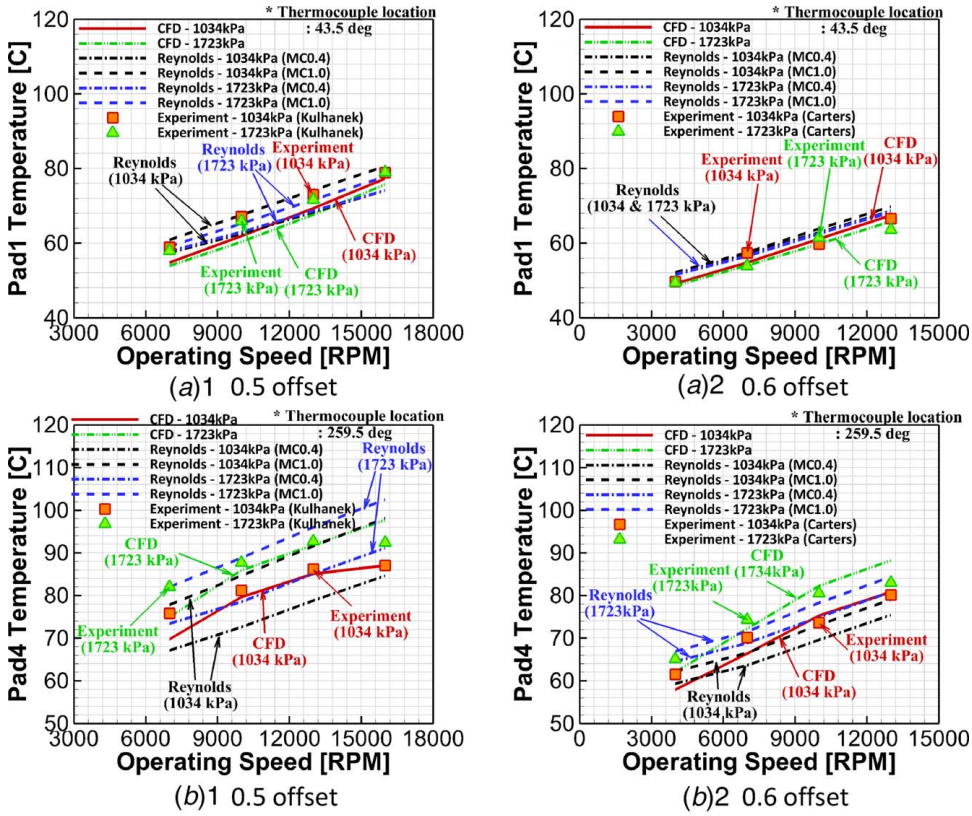

Fig. 13 Static results comparison (2): (*a*) pad 1 temperature at trailing edge and (*b*) pad 4 temperature at trailing edge

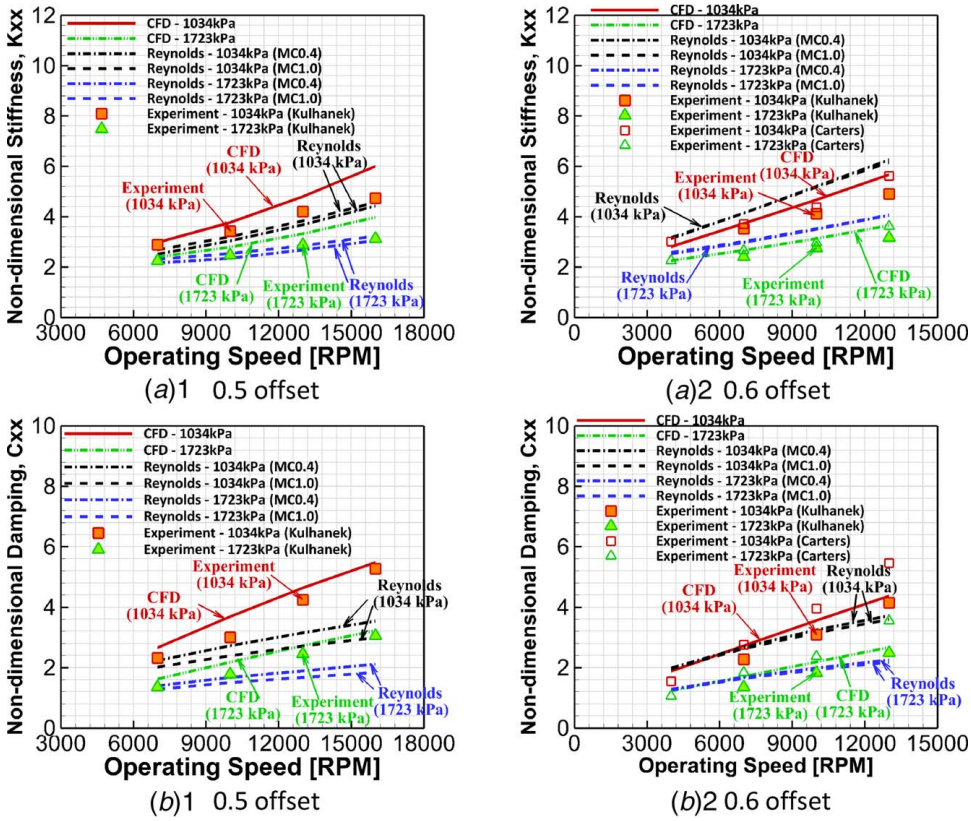

Fig. 14 Dynamic results comparison (1): (*a*) non-dimensional direct stiffness, Kxx, and (*b*) non-dimensional direct damping, Cxx

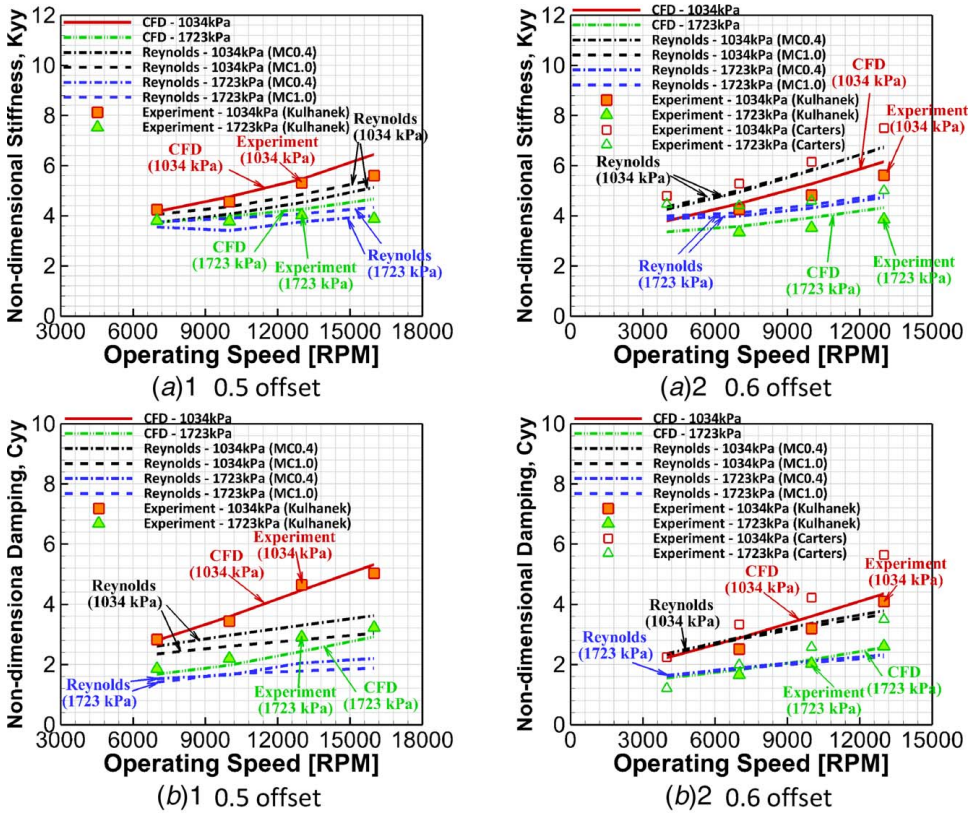

Fig. 15 Dynamic results comparison (2): (*a*) non-dimensional direct stiffness, Kyy, and (*b*) non-dimensional direct damping, Cyy

Table 8 Percent changes in Reynold model dynamic coefficients from including pad flexibility at 13,000 rpm

	1034 kPa		1723 kPa	
	0.5 offset	0.6 offset	0.5 offset	0.6 offset
Kxx	+2.5	+1.2	−1.3	−2.1
Kyy	+1.5	−0.1	−1.7	−2.9
Cxx	−3.3	−4.6	−7.3	−8.3
Cyy	−4.5	−6.9	−8.1	−9.8

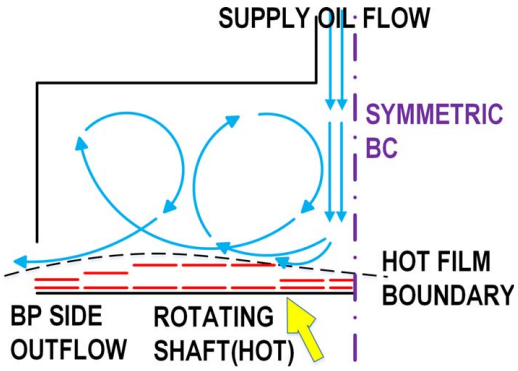

Fig. 16 Flow behavior along the bearing length

deviations due to pad flexibility effect. The stiffness is seen to either increase or decrease depending on load and offset conditions. The damping is seen to always decrease, and the reductions are more significant in higher load and offset conditions.

The relative benefits of the CFD approach over the Reynolds approach are summarized as follows:

(1) Improved supply flowrate prediction.
(2) Figure 13(*b-1*) shows that the maximum pad temperature in the Reynolds model is quite different for MC values of 0.4 and 1.0. This indicates the considerable result uncertainty due to MC uncertainty and that CFD removes the uncertainty.
(3) Figures 14(*a*) and 15(*a*) show that CFD provides better stiffness prediction than the Reynolds model except at 16,000 rpm with 0.5 offset.
(4) Figures 14(*b*) and 15(*b*) show that the Reynolds model has significant errors for the damping coefficient prediction when compared with the CFD simulation. Both MC extremes yield poor agreement. A more detailed study shows that the cause of the error in the Reynolds model is due to the fact that the radial and axial temperature distributions are neglected at the fluid-film leading-edge temperature.

5 Limitation of the Conventional Approach

The conventional Reynolds approach utilizes a bulk flow, mixing theory to determine an approximate uniform temperature at the inlet of each pad that depends on the MC selected, prior pad exit

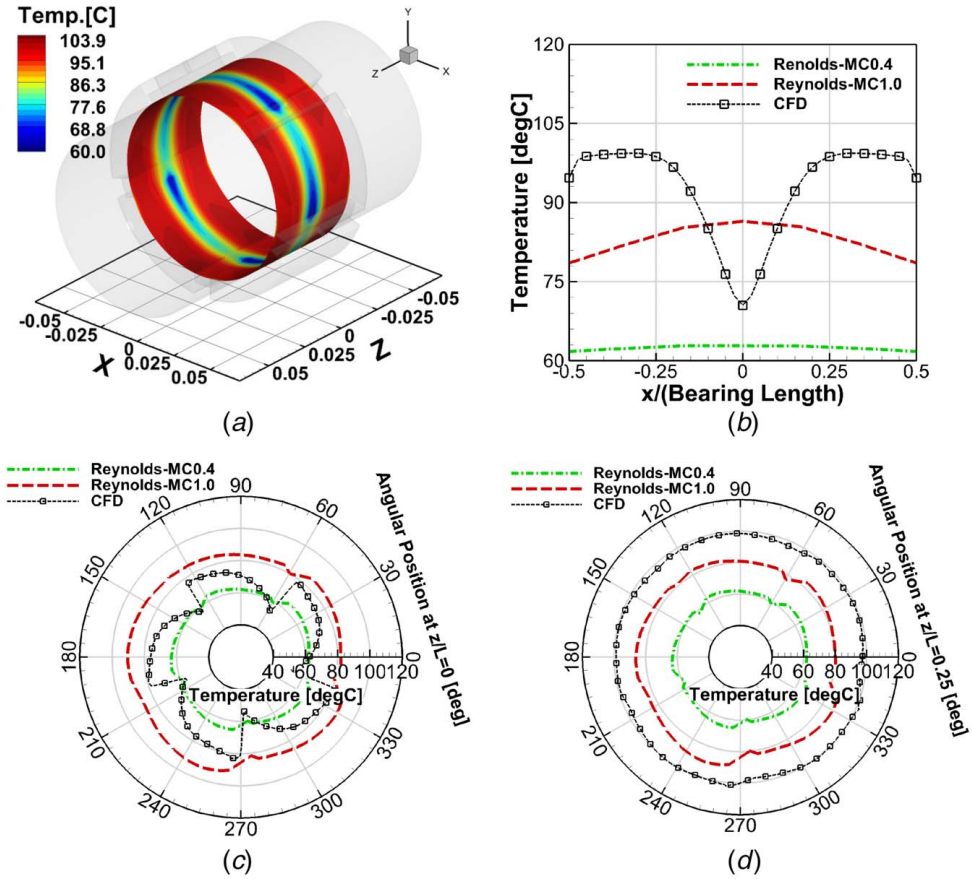

Fig. 17 Oil film temperature distribution at the shaft surface (15,000 rpm): (*a*) contour, (*b*) circumferential average value along the bearing length, (*c*) at *z*/*L* = 0, and (*d*) at *z*/*L*=0.25

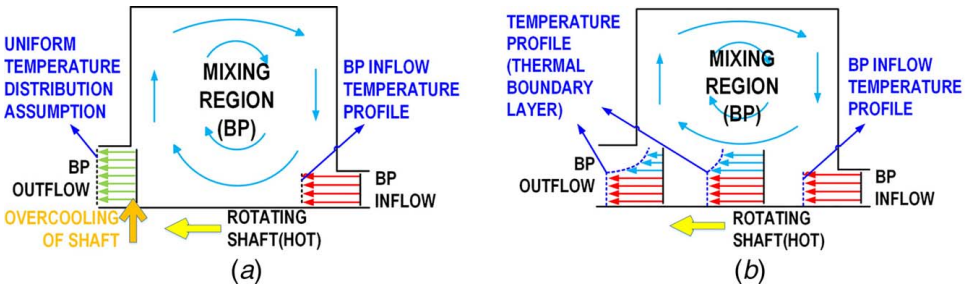

Fig. 18 Radial temperature distribution between pads: (*a*) Reynolds and (*b*) CFD

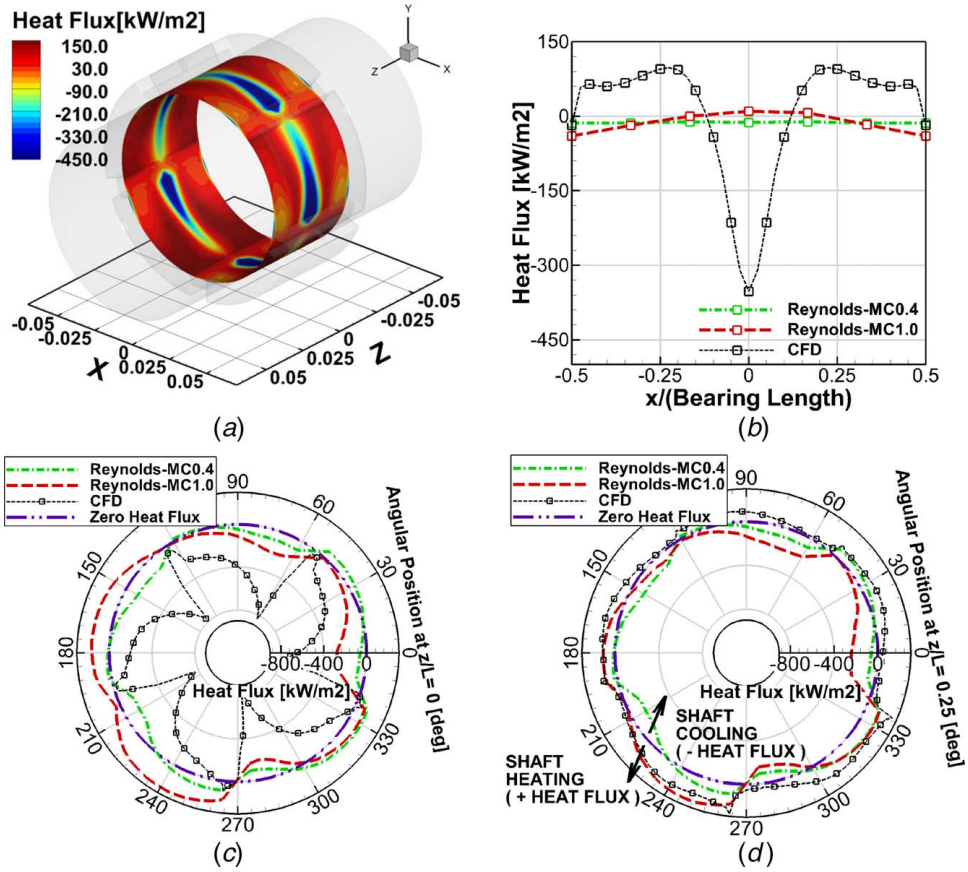

Fig. 19 Journal surface heat flux distribution (15,000 rpm): (*a*) contour, (*b*) circumferential average value along the bearing length, (c) at $z/L = 0$, and (*d*) at z/L=0.25

temperatures and flowrates, and supply oil flowrates and temperatures. References [51,52] indicated that a weakness of the conventional, Reynolds MC approach was in the assumption of uniform inlet temperatures at the pad inlets. Here, we utilize the results of cases Reynolds-MC0.4, Reynolds-MC1.0, and CFD in Sec. 3 to illustrate how pad inlet temperatures radically depart from the uniform temperature assumption, based on detailed 3D modeling of BP thermal flows with CFD.

Figure 16 depicts how the supplied oil enters the BP region and is exhausted through the BP side outlet. The cooler supply oil penetrates the hot oil film due to its high pressure (Nozzle effect) and also flows out pushing the film at the BP side outlet. Mixing is the strongest near the nozzle and at the side outlet, which results in lower temperature at these locations. The CFD results in Figs. 17(*a*) and 17(*b*) confirm the lowering of oil temperatures near the shaft surface at these locations. However, the conventional approach cannot predict these thermal-fluid features near the nozzle and the resulting axial temperature distribution at the inlet. Instead, it erroneously predicts higher temperatures near the mid-span, which CFD predicts to be the cooler region.

The Reynolds model shows fairly uniform trends along the bearing length ($z/L = 0$, $z/L = 0.25$). However, the CFD predictions vary in the axial direction, as shown by comparing Figs. 17(*c*) and 17(*d*). The temperatures at the middle of the bearing ($z/L = 0$) have sudden drops at pad leading edges and gradual increases from leading to trailing edges, as shown in Fig. 17(*c*). The temperatures differ considerably between the two models in Fig. 17(*c*) and the maximum CFD predicted temperatures occur at the end of the bearing, away from the nozzle, as shown in Fig. 17(*d*).

Another weakness of the conventional approach is the assumption of a uniform temperature profile in the radial direction at each pad inlet, as obtained from mixing theory and depicted in Fig. 18(*a*). In contrast, the CFD results show that the hot oil carryover temperature persists into the leading edge of the next pad, along with a thermal boundary layer above it, as depicted in Fig. 18(*b*). Thus, the film temperature in contact with the journal

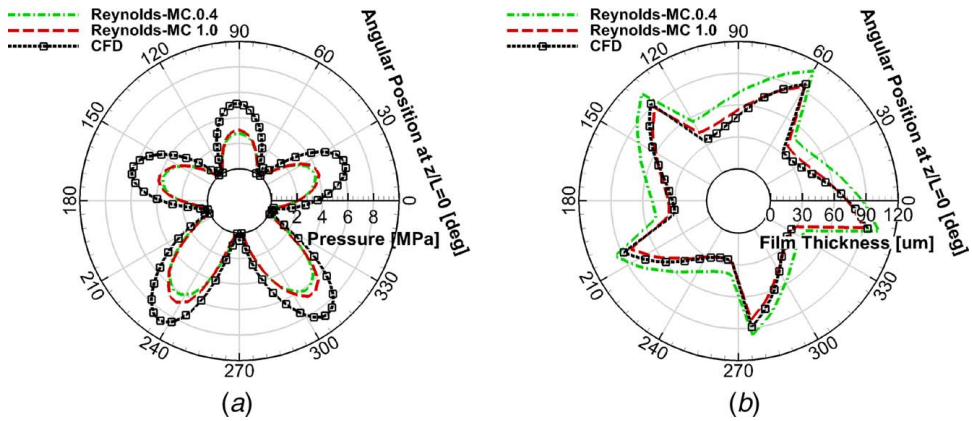

Fig. 20 Pressure and film thickness distribution at shaft surface (15,000 rpm): (*a*) pressure and (*b*) film thickness

may be much higher than the mixing temperature. The upper part of the BP inflow in the CFD model is first exposed to the cooling effect mainly by thermal diffusion, as illustrated in Fig. 18(*b*). The thermal boundary layer is developed in the process. The uniform, cooler inlet mixing temperature assumption of the Reynolds model forms a significantly different heat flux field on the entire journal surface, which depends on the radial temperature gradient and the thermal conductivity. The journal heat flux distribution may be highly dependent on the MC.

The mixing model uniform temperature profile causes a decrease in the oil temperature at the shaft surface after passing through the BP. Therefore, negative heat flux (shaft cooling) is predicted at most leading edges of the Reynolds model except for the pad 3 (132–192 deg) with the MC 1.0 and pad 4 (204–264 deg) with the MC 1.0 or MC 0.4, as shown in Figs. 19(*c*) and 19(*d*). On the contrary, all cooling is made adjacent to the bearing mid-span region ($z/L = -0.125$–0.125) in the CFD model, due to the nozzle effect, as shown in Figs. 19(*b*) and 19(*c*), and all heating process occurs at both bearing side regions ($z/L = -0.125$ to -0.5, 0.125 to 0.5). Note that the heating dominant region of the CFD model is wider than the dominant cooling region in Fig. 19(*b*).

The difference between the heat flux distributions causes an under-prediction of shaft temperatures in the Reynolds model. Both the Reynolds and CFD models show substantial cooling occurs at the Pad 1 (348–48 deg), 2 (60–120 deg), and 5 (276–336 deg), and intense heating takes place at the Pad 4 (204–264 deg). The under-predicted shaft temperature in the Reynolds model yields a thicker film thickness than that in the CFD model, as shown in Fig. 20(*b*). Accordingly, the CFD predicted pressures are higher than their Reynolds counterparts.

Regardless of its small volumetric portion, the BP region with its 3D physics produces a complex MC distribution along the bearing axial direction, and radial temperature distribution at the pad inlet. Finally, the two-dimensional temperature distribution at the pad inlet leads to very different temperature, pressure, heat flux, dynamic viscosity, and film thickness fields compared with the conventional approach. This is the reason that several results of the Reynolds model deviate from the CFD results in Sec. 3, even if adjusting MC values from 0.4 to 1.0.

6 Summary and Conclusion

This paper is an extension of the prior work [51,52] for TEHD CFD modeling of a TPJB. The previous study presented modeling methodology with: (1) multiphase flow, (2) thermal-fluid, (3) transitional turbulence, and (4) thermal deformation of the shaft and pads. The pad flexibility effect, which is known to affect TPJB damping significantly, was not included. The present work advanced the TEHD CFD TPJB model by inclusion of multiple-mode pad flexibility effect and presentation of the corresponding methodology. Formulas for the total perturbed shaft and pad displacement distributions on the mesh deformation boundaries are provided for calculating stiffness coefficients.

Formulas for the distributed velocity perturbations for computing damping coefficient were derived and are applied in the fluid film control volumes. Computation time reduction was addressed in the areas of effective pad mode selection, solution procedures, and choice of numerical approach. The advanced TEHD CFD TPJB model was validated by comparing it with the experimental work from the literature.

Finally, limitations of the BP mixing assumption of the conventional Reynolds TPJB modeling approach were identified by comparing results from the CFD and Reynolds models. Specifically, axial and circumferential distributions of pressure, temperature, heat flux, dynamic viscosity, and film thickness were contrasted between the CFD and conventional Reynolds approach.

Key conclusions of the paper include the following:

- An initial check on the TEHD CFD model was performed to compare its predictions with a TEHD Reynolds solution when the detailed BP thermal flow field is ignored and instead represented by pad thermal and pressure boundary conditions. The thin film only model is known to be solved with high accuracy by the TEHD Reynold approach, so its excellent agreement with the TEHD CFD model provided a strong means of validation for the latter approach.
- The BP regions were included with either a complex 3D CFD model in the TEHD CFD approach, or a highly simplified bulk flow Mixing model in the TEHD Reynolds approach. The CFD results were either bounded by the extremes of the Mixing approach results (MC = 0.4, 1.0) or lied outside of this range of results.
- Including pad flexibility had significant influence on eccentricity ratio (Max. +20.6%), stiffness (−16.4%), and damping coefficient (Max. −16.6%).
- A comparison of results from the TEHD CFD model showed very good agreement with experimental results obtained from the literature, for supply pressure, supply flowrate, eccentricity ratio, pad temperature, stiffness, and damping coefficient. The agreement was significantly better than that between the conventional TEHD Reynolds approach and the experimental results, except for the *x*-direction bearing stiffness.
- The assumptions of the conventional TEHD Reynolds approach include invariance of the temperature in the radial and axial directions at each pad inlet. A study was performed utilizing the TEHD CFD approach with detailed 3D BP models as a benchmark to investigate the validity of the

TEHD—Reynolds leading edge temperature assumptions. It was confirmed that these assumptions were significantly violated and could result in pressure, temperature, dynamic viscosity, heat flux, and film thickness distribution significantly different from the TEHD CFD results.

- It is remarkable that including the three-dimensional BP model significantly affected predictions of bearing performance.

Acknowledgment

The authors appreciatively acknowledge the funding for this research from the Texas A&M Turbomachinery Research Consortium (TRC) and the Texas A&M High-Performance Research Computing Center (HPRC).

Conflict of Interest

There are no conflicts of interest.

Nomenclature

$\{f\}$ = force vector, N
h = film thickness, m
k = stiffness, N/m
$[k]$ = stiffness matrix, N/m
m = mass, kg
$[m]$ = mass matrix, kg
p = pressure, Pa
r = volume fraction
t = time, s
u = velocity, m/s
$\{x\}$ = total displacement vector, m
F = force in modal coordinate, N
$\{F\}$ = force vector in modal coordinate, N
$[K]$ = stiffness matrix in modal coordinate, N/m
$[M]$ = mass matrix in modal coordinate, m
R = radius, m
T = temperature, °C
$[\hat{c}_{JJ}]$ = frequency reduced damping coefficient matrix, Ns/m
$[\hat{k}_{JJ}]$ = frequency reduced stiffness coefficient matrix, N/m
k_f = turbulent kinetic energy, m^2/s^2
m_{pr} = preload
s_C = mass source per unit volume, kg/m^3
s_E = energy source per unit volume, J/m^3 s
s_M = momentum source per unit volume, N/m^3
x_0 = initial x position in global coordinate, m
y_0 = initial y position in global coordinate, m
C_p = specific heat, J/kg K
I_T = pad moment of inertia, kg m^2
Cl = clearance, m
γ = turbulence intermittency
δ_{dec} = log decrement
Δm_{pb} = modal displacement perturbation, m
$\Delta \dot{m}_{pb}$ = modal velocity perturbation, m/s
Δp_{pb} = pad pivot displacement perturbation, m
$\Delta \dot{p}_{pb}$ = pad pivot velocity perturbation, m
Δx_{pb} = shaft x displacement perturbation, m
$\Delta \dot{x}_{pb}$ = shaft x velocity perturbation, m
ΔX_{se} = total nodal shaft displacement at equilibrium state, m
ΔX_{pe} = total nodal pad displacement at equilibrium state, m
Δy_{pb} = shaft y displacement perturbation, m
$\Delta \dot{y}_{pb}$ = shaft y velocity perturbation, m
$\Delta \delta_{pb}$ = pad angular displacement perturbation, deg
$\Delta \dot{\delta}_{pb}$ = pad angular velocity perturbation, deg
θ_p = pad angular position, deg
λ = eigenvalue
$[\lambda]$ = eigenvalue matrix
ν = synchronous frequency, 1/s
$\{\xi\}$ = total displacement vector in modal coordinate, m
ρ = density, kg/m^3
$\{\phi\}$ = eigenvetor (mode shape)
$[\phi_M]$ = selected eigenvector matrix
ω = natural frequency, 1/s
ω_f = turbulent frequency, 1/s
Ω_s = shaft speed, rad/s

Superscript

j = pad number index

Subscripts

b = bearing
brg = full bearing
e = equilibrium state
f = fluid
F = flexible pad
i = node number index or rotor eigenvalue number index
I = velocity (u,v,w) index
J = journal
k = mode number index (or l)
l = liquid phase
p = pad
pe = pad equilibrium
pvt = pivot
R = rigid pad
s = shaft
se = shaft equilibrium
v = vapor phase

References

[1] Lund, J., 1964, "Spring and Damping Coefficients for the Tilting-Pad Journal Bearing," ASLE Trans., **7**(4), pp. 342–352.
[2] Tieu, A., 1973, "Oil-Film Temperature Distribution in an Infinitely Wide Slider Bearing: An Application of the Finite-Element Method," J. Mech. Eng. Sci., **15**(4), pp. 311–320.
[3] Ettles, C. M. M., 1980, "The Analysis and Performance of Pivoted Pad Journal Bearings Considering Thermal and Elastic Effects," ASME J. Lubr. Tech., **102**(2), pp. 182–191.
[4] Kirk, R., and Reedy, S., 1988, "Evaluation of Pivot Stiffness for Typical Tilting-Pad Journal Bearing Designs," ASME J. Vib. Acoust. Stress Reliab. Des., **110**(2), pp. 165–171.
[5] Knight, J. D., and Barrett, L. E., 1988, "Analysis of Tilting-Pad Journal Bearing With Heat Transfer Effects," ASME J. Tribol., **110**(1), pp. 128–133.
[6] Brugier, D., and Pascal, M. T., 1989, "Influence of Elastic Deformations of Turbo-Generator Tilting Pad Bearings on the Static Behavior and on the Dynamic Coefficients in Different Designs," ASME J. Tribol., **111**(2), pp. 364–371.
[7] Earles, L., Amentrout, R., and Palazzolo, A., 1990, "A Finite Element Approach to Pad Flexibility Effects in Tilt Pad Journal Bearings-Part I: Single Pad Analysis," ASME J. Tribol., **112**(2), pp. 169–176.
[8] Taniguchi, S., Makino, T., Takeshita, K., and Ichimura, T., 1990, "A Thermohydrodynamic Analysis of Large Tilting-Pad Journal Bearing in Laminar and Turbulent Flow Regimes With Mixing," ASME J. Tribol., **112**(3), pp. 542–550.
[9] Fillon, M., Bligoud, J. C., and Frene, J., 1992, "Experimental Study of Tilting-Pad Journal Bearings-Comparison With Theoretical Thermoelastohydrodynamic Results," ASME J. Tribol., **114**(3), pp. 579–588.
[10] Kim, J., Palazzolo, A. B., and Gadangi, R. K., 1994, "TEHD Analysis for Tilting-Pad Journal Bearings Using Upwind Finite Element Method," Tribo. Trans., **37**(4), pp. 771–783.
[11] Kim, J., Palazzolo, A., and Gadangi, R., 1995, "Dynamic Characteristics of TEHD Tilt Pad Journal Bearing Simulation Including Multiple Mode Pad Flexibility Model," ASME J. Vib. Accoust., **117**(1), pp. 123–135.
[12] Gadangi, R., and Palazzolo, A., 1995, "Transient Analysis of Tilt Pad Journal Bearings Including Effects of Pad Flexibility and Fluid Film Temperature," ASME J. Tribol., **117**(2), pp. 302–307.
[13] Desbordes, H., Wai, C. C. H., Fillon, M., and Frene, J., 1995, "The Effects of Three-Dimensional Pad Deformations on Tilting-Pad Journal Bearings Under Dynamic Loading," ASME J. Tribol., **117**(3), pp. 379–384.
[14] Fillon, M., and Khonsari, M., 1996, "Thermohydrodynamic Design Charts for Tilting-Pad Journal Bearings," ASME J. Tribol., **118**(1), pp. 232–238.
[15] Haugaard, A. M., and Santos, I. F., 2010, "Multi-Orifice Active Tilting-Pad Journal Bearings-Harnessing of Synergetic Coupling Effects," Tribol. Int., **43**(8), pp. 1374–1391.
[16] Rindi, A., Rossin, S., Conti, R., Frilli, A., Galardi, E., Meli, E., Nocciolini, D., and Pugi, L., 2015, "An Efficient Quasi-Three-Dimensional Model of Tiling Pad

Journal Bearing for Turbomachinery Applications," ASME J. Vib. Accoust., **137**(6), p. 061013.
[17] Dang, P. V., Chatterton, S., Pennacchi, P., and Vania, A., 2016, "Numerical Investigation of the Effect of Manufacturing Errors in Pads on the Behavior of Tilting-Pad Journal Bearings," Proc. Inst. Mech. Eng. Part J, J. Eng. Tribol., **232**(4), pp. 480–500.
[18] Lee, D., Sun, K., Kim, B., and Kang, D., 2017, "Thermal Behavior of a Worn Tilting Pad Journal Bearing: Thermohydrodynamic Analysis and Pad Temperature Measurement," Tribo. Trans., **61**(6), pp. 1074–1083.
[19] Mehdi, S. M., Jang, K., and Kim, T., 2018, "Effects of Pivot Design on Performance of Tilting pad Journal Bearings," Tribol. Int., **119**, pp. 175–189.
[20] Arihara, H., Kameyama, Y., Baba, Y., and Andes, L. S., 2018, "A Thermoelastohydrodynamic Analysis for the Static Performance of High-Speed —Heavy Load Tilting-Pad Journal Bearing Operating in the Turbulent Flow Regime and Comparisons to Test Data," ASME J. Eng. Gas Turbines Power, **141**(2), p. 021023.
[21] San Andres, L., and Tao, Y., 2013, "The Role of Pivot Stiffness on the Dynamic Force Coefficients of Tilting Pad Journal Bearings," ASME J. Eng. Gas Turbines Power, **135**(11), p. 112505.
[22] San Andres, L., Tao, Y., and Li, Y., 2015, "Tilting Pad Journal Bearings: On Bridging the Hot Gap Between Experimental Results and Model Predictions," ASME J. Eng. Gas Turbines Power, **137**(2), p. 022505.
[23] San Andres, L., and Li, Y., 2015, "Effect of Pad Flexibility on the Performance of Tilting Pad Journal Bearings—Benchmarking a Predictive Model," ASME J. Eng. Gas Turbines Power, **137**(12), p. 122503.
[24] San Andres, L., Koo, B., and Hemmi, M., 2018, "A Flow Starvation Model for Tilting Pad Journal Bearings and Evaluation of Frequency Response Functions: A Contribution Toward Understanding the Onset of Low Frequency Shaft Motions," ASME J. Eng. Gas Turbines Power, **140**(5), p. 052506.
[25] Abdollahi, B., and Andres, L. S., 2018, "Improved Estimation of Bearing Pads' Inlet Temperature: A Model for Lubricant Mixing at Oil Feed Ports and Validation Against Test Data," ASME J. Tribol., **141**(3), p. 031703.
[26] Hagemann, T., Zeh, C., Prölß, M., and Schwarze, H., 2017, "The Impact of Convective Fluid Inertia Forces on Operation of Tilting-Pad Journal Bearings," Int. J. Rotating Mach., **2017**, pp. 1–12. Article ID 5683763.
[27] Hagemann, T., and Schwarze, H., 2018, "A Model for Oil Flow and Fluid Temperature Inlet Mixing in Hydrodynamic Journal Bearings," ASME J. Tribol., **141**(2), p. 021701.
[28] Mermertas, U., Hagemann, T., and Brichart, C., 2018, "Optimization of a 900 mm Tilting-Pad Journal Bearing in Large Steam Turbines by Advanced Modeling and Validation," ASME J. Eng. Gas Turbine Power, **141**(2), p. 021033.
[29] Hagemann, T., and Schwarze, H., 2019, "Theoretical and Experimental Analyses of Directly Lubricated Tilting-Pad Journal Bearings With Leading Edge Groove," ASME J. Eng. Gas Turbines Power, **141**(5), p. 051010.
[30] Suh, J., and Palazzolo, A., 2015, "Three-Dimensional Dynamic Model of TEHD Tilting-Pad Journal Bearing-Part I: Theoretical Modeling," ASME J. Tribol., **137**(4), p. 041703.
[31] Suh, J., and Palazzolo, A., 2015, "Three-Dimensional Dynamic Model of TEHD Tilting-Pad Journal Bearing-Part II: Parametric Studies," ASME J. Tribol., **137**(4), p. 041704.
[32] Tong, X., and Palazzolo, A., 2016, "Double Overhung Disk and Parameter Effect on Rotordynamic Synchronous Instability—Morton Effect—Part II: Occurrence and Prevention," ASME J. Tribol., **139**(1), p. 011706.
[33] Tong, X., and Palazzolo, A., 2017, "Measurement and Prediction of the Journal Circumferential Temperature Distribution for the Rotordynamic Morton Effect," ASME J. Tribol., **140**(3), p. 031702.
[34] Gaines, J. E., and Childs, D. W., 2016, "The Impact of Pad Flexibility on the Rotordynamic Coefficients of Tilting-Pad Journal Bearings," ASME J. Eng. Gas Turbines Power, **138**(8), p. 082501.
[35] Wygant, K. D., Flack, R. D., and Barrett, L. E., 1999, "Influence of Pad Pivot Friction on Tilting Pad Journal Bearing Measurement—Part I: Static Operating Conditions," Tribol. Trans., **42**(1), pp. 210–215.
[36] Wygant, K. D., Flack, R. D., and Barrett, L. E., 1999, "Influence of Pad Pivot Friction on Tilting Pad Journal Bearing Measurement—Part II: Dynamic Coefficients," Tribol. Trans., **42**(1), pp. 250–256.
[37] Pettinato, B. C., and De Choudhury, P., 1999, "Test Results of Key and Spherical Pivot Five-Shoe Tilt Pad Journal Bearings—Part I: Performance Measurement," Tribol. Trans., **42**(3), pp. 541–547.
[38] Pettinato, B. C., and De Choudhury, P., 1999, "Test Results of Key and Spherical Pivot Five-Shoe Tilt Pad Journal Bearings—Part II: Dynamic Measurements," Tribol. Trans., **42**(3), pp. 675–680.
[39] Kim, S. G., and Kim, K. W., 2008, "Influence of Pad-Pivot Friction on Tilting Pad Journal Bearing," Tribol. Int., **41**(8), pp. 694–703.
[40] Kim, S., and Palazzolo, A., 2019, "Pad–Pivot Friction Effect on Nonlinear Response of a Rotor Supported by Tilting-Pad Journal Bearings," ASME J. Tribol., **141**(9), p. 091701.
[41] Lu, X., Khonsari, M. M., and Gelink, E. R., 2006, "The Stribeck Curve: Experimental Results and Theoretical Prediction," ASME J. Tribol., **128**(4), pp. 789–794.
[42] Guo, Z., Toshio, H., and Gorden, R., 2005, "Application of CFD Analysis for Rotating Machinery Part1: Hydrodynamic, Hydrostatic Bearings and Squeeze Film Damper," ASME J. Eng. Gas Turbines Power, **127**(4), pp. 445–451.
[43] Liu, H., Xu, H., Ellison, P. J., and Jin, Z., 2010, "Application of Computational Fluid Dynamics and Fluid-Structure Interaction Method to the Lubrication Study of a Rotor-Bearing System," Tribol. Lett., **38**, pp. 324–336.
[44] Li, Q., Liu, S., Pan, X., and Zheng, S., 2012, "A new Method for Studying the 3D Transient Flow of Misaligned Journal Bearings in Flexible Rotor-Bearing Systems," J. Zhejiang Univ. Sci. A, **13**(4), pp. 293–310.
[45] Lin, Q., Wei, Z., Wang, N., and Chen, W., 2013, "Analysis on the Lubrication Performances of Journal Bearing System Using Computational Fluid Dynamics and Fluid-Structure Interaction Considering Thermal Influence and Cavitation," Tribol. Int., **64**, pp. 8–15.
[46] Li, M., Gu, C., Pan, X., Zheng, S., and Li, Q., 2016, "A new Dynamic Mesh Algorithm for Studying the 3D Transient Flow Field of Tilting pad Journal Bearings," Proc. Inst. Mech. Eng. Part J: J. Eng. Tribol., **230**(12), pp. 1470–1482.
[47] Armentrout, R. W., He, M., Haykin, T., and Reed, A., 2017, "Analysis of Turbulence and Convective Inertia in a Water-Lubricated Tilting-Lubricated Tilting-Pad Journal Bearing Using Conventional and CFD Approaches," Tribol. Trans., **60**(6), pp. 1129–1147.
[48] Crone, P., Almqvist, A., and Larsson, R., 2018, "Thermal Turbulent Flow in Leading Edge Grooved and Conventional Tilting Pad Journal Bearing Segments-A Comparative Study," Lubricants, **6**(4), p. 97.
[49] Ding, A., Ren, X., Li, X., and Gu, C., 2018, "Friction Power Analysis and Improvement for a Tilting-pad Journal Bearing Considering air Entrainment," Appl. Therm. Eng., **145**(25), pp. 763–771.
[50] Hagemann, T., Zeh, C., and Schwarze, H., 2019, "Heat Convection Coefficients of a Tilting-pad Journal Bearing with Directed Lubrication," Tribol. Int., **136**, pp. 114–126.
[51] Yang, J., and Palazzolo, A., 2019, "3D Thermo-Elasto-Hydrodynamic CFD Model of a Tilting Pad Journal Bearing-Part I: Static Response," ASME J. Tribol., **141**(6), p. 061702.
[52] Yang, J., and Palazzolo, A., 2019, "3D Thermo-Elasto-Hydrodynamic CFD Model of a Tilting Pad Journal Bearing-Part II: Dynamic Response," ASME J. Tribol., **141**(6), p. 061703.
[53] Carter, C. R., 2007, "Measurement and Predicted Rotordynamic Coefficients and Static Performance of a Rocker-Pivot Tilt Pad Bearing in Load-On-Pad and Load-Between-Pad Configurations," M.S. thesis, Mechanical Engineering, Texas A&M University, College Station, TX.
[54] Kulhanek, C. D., 2010, "Dynamic and Static Characteristics of a Rocker-Pivot, Tilting-Pad Bearing With 50% and 60% Offsets," M.S. thesis, Mechanical Engineering, Texas A&M University, College Station, TX.
[55] Palazzolo, A., 2016, *Vibration Theory and Applications With Finite Elements and Active Vibration Control*, Wiley, Chichester, UK.